UNIVERSIDAD POLITECNICA DE VALENCIA

DEPARTAMENTO DE COMUNICACIONES

Máster Universitario en Tecnologías, Sistemas y Redes de Comunicaciones

Study of Second-Order Non-Linearity in Strained Silicon for All-Optical Switching

Author: Steven Van Roye

Supervisor 1: Prof. Pablo Sanchis

Supervisor 2: Irene Olivares

Start date: 01-02-2016

Work place: Valencia Nanophotonics Technology Center (NTC)

Objectives – The objective of the master thesis is to study the second-order non-linearity in silicon strained with a silicon nitride layer. The influence of performing annealing on this so-called strained silicon is examined. The use of strained silicon as an application in a Mach-Zehnder interferometer is examined.

Methodology – Recent research about strained silicon, together with experimental results, were studied in detail. Next, several simulations were performed to get an idea of the influence of annealing on the stress inside the silicon and silicon nitride, both at an interface between them and at a silicon waveguide structure strained with silicon nitride. Experiments were performed to verify the obtained simulation results.

Theoretical developments – The second-order non-linearity in silicon was studied, together with the diffusion models used in SILVACO, needed for the annealing procedure, and the basic working principle of a Mach-Zehnder interferometer. A figure of merit was defined, which value should be proportional to an induced Pockels effect.

Prototyping and lab work – Samples with an asymmetric Mach-Zehnder interferometer with high and low intrinsic compressive stresses were fabricated. On these samples, measurements were made to investigate the behavior of the interferometer when a voltage was applied to one arm of the interferometer. Next, an annealing was performed on the samples to see whether the annealing had an influence on the response of the interferometer.

Results – From the simulations, it was found that annealing improved the figure of merit in case the silicon nitride layer had an intrinsic tensile stress and it was reduced in case the silicon nitride had an intrinsic compressive stress. From the experiments, an improved response after annealing was observed for the Mach-Zehnder interferometer, although the used sample had a silicon nitride layer with an intrinsic compressive stress, which thus should reduce the figure of merit and hence the response. Clear evidence of the Pockels effect was not seen, however, the presence of the free-carrier plasma effect was clearly seen in the response of the Mach-Zehnder interferometer.

Future lines – Simulations with respect to the free-carrier plasma effect should be carried out to fully understand the experimental results that were obtained. A sample with a silicon nitride layer with an intrinsic tensile stress should be fabricated and the response should be measured, both before and after annealing, to see whether the response improves or not.

Publications – Publication for the Spanish Nanophotonics Conference (CEN) 2016 in Valencia. The corresponding paper is included in the annex at the end of the master thesis.

Abstract – Silicon photonics technology is compatible with CMOS processes and fabrication infrastructure. It gives us all the advantages that photonics has with respect to electronics. However, silicon has certain disadvantages, amongst which the absence of an electro-optic effect, which manifests itself in the fact that it cannot be used for optically active devices relying on second-order nonlinear effects. It was demonstrated however that silicon strained with a silicon nitride layer breaks the centro-symmetric crystal structure of silicon and induces a second-order non-linearity in it. Therefore, it could be used for active devices relying on the Pockels effect, such as a Mach-Zehnder interferometer. The stress in strained silicon and the influence of annealing on the stress was examined. To this end, a figure of merit was defined, which value should be proportional to the induced non-linearity. It was found that annealing improved this figure of merit in case of a silicon nitride layer with an intrinsic tensile stress and reduced it in case of an intrinsic compressive stress. A higher annealing temperature thus leads to an improved figure of merit and hence non-linearity only in case of an intrinsic tensile stress. Experimental results on a Mach-Zehnder interferometer made of strained silicon with an intrinsic compressive stress of the silicon nitride however showed an improvement of the response of the interferometer after annealing. The Pockels-effect was not clearly observed, but the influence of the free-carrier plasma effect was clearly present in the response. For a lower intrinsic compressive stress, neither the Pockels-effect nor the free-carrier plasma effect were observed.

Author: Steven Van Roye, email: Steven.VanRoye@UGent.be
Supervisor 1: Prof. Pablo Sanchis, email: pabsanki@dcom.upv.es
Supervisor 2: Irene Olivares, email: irolsan@upv.es
End date: 11-07-2016

Contents

1 Introduction

Silicon (Si) photonics technology is compatible with CMOS processes and fabrication infrastructure. This means that we are able to produce devices at a high volume with relatively low cost. Also, the devices are highly integrated and are scalable [1]. Furthermore, the use of Si and CMOS gives us all the advantages that photonics has with respect to electronics, namely higher speed of operation, lower power consumption and immunity to electrical noise. Although the use of Si has a number of advantages, such as transparency in the telecom range and low cost, it also has a number of disadvantages, such as the lack of an efficient light emission and the lack of an electro-optic effect [2]. This absence of an electro-optic effect manifests itself in the fact that Si cannot be used for modulators, and more general that Si cannot be used for the fabrication of optically active devices relying on second-order nonlinear effects such as the Pockels effect [3, 4], because it only exhibits a third-order optical non-linearity due to its crystalline inversion symmetry, i.e. due to the centro symmetry of its lattice structure, it lacks a second-order optical non-linearity (or second-order susceptibility $\chi^{(2)}$) [5, 6].

From the following compact mathematical explanation, we can see that the second-order nonlinear susceptibility disappears in centro-symmetric materials such as Si. In second-order nonlinear optical processes, two light waves with electric field vectors $\boldsymbol{E_1}$ and $\boldsymbol{E_2}$ generate the nonlinear polarization $\boldsymbol{P^{(2)}}$, which is given by

$$\boldsymbol{P^{(2)}} = \epsilon_0 \chi^{(2)} \boldsymbol{E_1} \boldsymbol{E_2}. \tag{1}$$

In the most general case, the $\chi^{(2)}$ tensor contains 27 elements. However, making use of the Kleinmann symmetry condition and Kleinmann convention allows us to simplify the expression for the susceptibility significantly. The final result is

$$d_{\alpha_\mu \alpha} = \begin{bmatrix} d_{11} & d_{12} & d_{13} & d_{14} & d_{15} & d_{16} \\ d_{16} & d_{22} & d_{23} & d_{24} & d_{14} & d_{12} \\ d_{15} & d_{24} & d_{33} & d_{23} & d_{13} & d_{14} \end{bmatrix}, \tag{2}$$

in which $d_{\alpha_\mu \alpha} = d_{\alpha_\mu \alpha_1 \alpha_2} = \frac{1}{2} \chi^{(2)}_{\alpha_\mu \alpha_1 \alpha_2}$. Applying Neumann's principle on this table, which tells us that the symmetry elements of the tensor associated with a material property of a crystal must include all the symmetry properties of the point group of the crystal, it can be simplified even more. For the special case of Si, which has a centro-symmetric crystal structure, we find that all the elements of this matrix are zero. Hence, Si does not exhibit a second-order optical nonlinearity. Therefore, Si cannot be used in second-order nonlinear optical processes.

Nevertheless, nonlinear active devices based on Si can be fabricated by exploiting its third-order nonlinearity $\chi^{(3)}$ or combining other nonlinear materials with Si (e.g. lithium niobate $LiNbO_3$ for optical modulators). However, both of these solutions have certain drawbacks. For the former, relatively high powers are required and they compete with nonlinear-loss mechanisms, such as two-photon absorption (TPA) and two-photon induced free-carrier absorption [6, 7], due to which the efficiency of these processes is limited [5]. Moreover, TPA creates a considerable population of free carriers, which in turn introduce

a severe absorption, due to which the mode index changes, which is an obstacle for practical applications of Si nonlinear devices [8]. With respect to combining other nonlinear materials with Si, although e.g. $LiNbO_3$ electro-optic (EO) modulators satisfy bandwidth, linearity and chirp requirements in fiber-optic transmission systems, the dimensions are relative big and hence the potential for dense integration is limited [9]. Therefore, the desire for exploiting the second-order non-linearity $\chi^{(2)}$ in Si for e.g. modulators is tremendous due to the aforementioned advantages of it.

1.1 Second-Harmonic Generation in Strained Silicon

As explained above, the crystal structure of Si inhibits us to exploit the second-order susceptibility for nonlinear active devices, simply because $\chi^{(2)}$ vanishes in centro-symmetric materials. However, it was found that a significant $\chi^{(2)}$ can be induced in Si in two ways. The first way was discovered by the fact that second-harmonic generation (SHG) was observed in reflection from a Si surface [10] or in diffusion from Si photonic crystal nanocavities [7]. The former was achieved by subjecting the Si interface to an inhomogeneous deformation as a result of ion implantation with subsequent pulsed-laser annealing, thermal oxidation or silicide film deposition on the surface. The latter was achieved by using a nanocavity surrounded by a photonic crystal and the second-order non-linearity was determined by the surface boundary between the Si and the holes of the photonic crystal. The second way in which a significant $\chi^{(2)}$ can be induced is by applying an inhomogeneous strain to Si by covering it with a straining layer (mostly silicon nitride (SiN)), due to which the crystal structure of Si (crystalline symmetry) can be broken [3–6,11,12]. Because this crystalline symmetry (more specifically its centro-symmetric crystal structure) was the factor responsible for the vanishing of $\chi^{(2)}$, breaking this will induce a non-zero $\chi^{(2)}$, due to which the so called strained Si can be used for optically active devices relying on this [13]. The most common active device is the Mach-Zehnder interferometer (MZI), which converts a phase modulation into an amplitude modulation, and makes use of the Pockels effect.

Experimental results of SHG in strained Si can be found in [6], in which they used silicon-on-insulator (SOI) waveguides with a stressing SiN on top of it as cladding. The thickness of this cladding layer was changed to alter the applied stress on the structure. This stress in turn induces a strain on the Si waveguide. To experimentally verify that the strained Si had an induced second-order non-linearity, a SHG experiment was performed, in which a 2.1 µm pump source was used. At the output of the waveguide, the transmitted signal not only consisted of the pump source, but also of a peak at 1.05 µm, which is the second-harmonic (SH) signal. Furthermore, performing a sweep over the pump wavelength, it was seen that the wavelength of this peak signal shifted linearly with the pump wavelength, which is expected for SHG. A last confirmation that this peak was due to SHG was found by observing a quadratic dependence of the peak power as a function of the pump power. As a next step, a power-conversion efficiency η from the pump signal to the SH signal was calculated such that $\chi^{(2)}$ could be extracted from this, with the result that values up to 40 pm/V could be achieved, comparable with the values known for $LiNbO_3$.

1.2 Second-Harmonic Generation in Silicon Nitride

Although lots of research is performed on inducing non-linearities in Si by straining it with SiN, also the non-linearities in SiN should be examined. This is needed to make sure that when non-linearities are measured in strained Si, such as SHG, it is in fact due to the Si and not due to the SiN. Therefore, in the following, several experiments of SHG in SiN-structures are discussed.

SiN is a widely used material in the SOI platform (SOI) due to multiple reasons : flexibility in the material composition and refractive index, low losses at wavelength regions of importance (such as the visible and near infrared) and in the same way as Si, it is compatible with CMOS processes [14]. Other interest for using SiN is related with all-optical switching (AOS) devices. In Si-based nonlinear resonant devices, the switching operations are dominated by free carrier non-linearity excited via two-photon absorption (TPA), due to which the response time is limited by the free carrier lifetime [15]. Using SiN, which has a large energy band gap, this TPA has a negligible value and the weaker but faster Kerr-non-linearity can be used. This was shown experimentally in [15], where SiN ring resonators were fabricated and a pump-probe experiment was performed, in which a continuous wave (CW) probe light was used to monitor the resonant transmission in time, while the resonant device was optically modulated by a pump light.

Next to the Kerr-non-linearity, which is a third-order non-linearity, also SHG can be observed in SiN, although the structure of SiN is thought to be amorphous and centro-symmetric, which thus should not exhibit a second-order nonlinear response. As shown in [16], a $\chi^{(2)}$ is induced by using an interface between two centro-symmetric materials, a SiN-core and a SiO_2-cladding. This interface breaks the bulk symmetry and hence a second-order non-linearity can arise there. In the experiment, a SiN ring resonator is fabricated and a pump source of 1554 nm was coupled into the ring, with the result that an output at the SH wavelength (777.1 nm) was observed. The effective susceptibility $\chi^{(2)}_{eff}$, measured from the conversion efficiency, was as high as 10^{-14} m/V. Note that the major difference with the SHG at the reflection of the surface of Si described previously is that in this case, a guided SH signal is present in the ring resonator and is coupled out through the bus waveguide.

Furthermore, strong SHG can be observed from SiN films grown on fused silica substrates using Plasma-Enhanced Chemical Vapor Deposition (PECVD) [14]. Here, samples with different thicknesses of the SiN were fabricated and illuminated with a 1064 nm laser source. At the output (transmission), a signal at 532 nm was present, which indeed is the SH signal. A quadratic dependence of the SHG intensity on the pump source was seen for several thicknesses of the SiN film. The intensities measured were much larger than those of other centro-symmetric dielectric materials, measured in reflection. Moreover, the dominant tensor component of the second-order susceptibility was around 2.5 pm/V, which is much larger than the one for the case of a SiN ring resonator, and even 3 times larger than the value for Potassium Dihydrogen Phosphate (KDP). Although the origin

of the response was not yet fully clear, the results suggested that the response was likely to be of bulk origin.

Another experiment which demonstrated SHG in SiN can be found in [17], where the experiment was performed in an amorphous silicon nitride (a-SiN:H) based microcavity. Here, the SH signal was found to be correlated with the resonance of the microcavity by measuring the intensity of the SH signal at a fixed pump wavelength as a function of the incidence angle of the pump source. From the theory of Fabry-Perot cavities, we know that increasing the incidence angle leads to a decrease in the resonance wavelength. When at a certain angle the incident wavelength of the pump source was at resonance in the cavity, the SH signal intensity showed a maximum. The use of the cavity resulted in an enhanced surface SHG.

In summary, the interface between the Si and SiN could give rise to SHG in SiN. In addition, thin SiN films grown on the Si using PECVD could exhibit strong SHG. Both should be taken into account when SHG is observed in a strained Si sample, since the observed SHG could then origin from the Si, from the SiN, or a combination of both.

1.3 Free-Carrier Plasma Effect

As explained in section 1.1, a significant $\chi^{(2)}$ can be induced in Si by straining it with a SiN-layer, such that it can be used for e.g. an MZI relying on the Pockels effect. Although a linearity of the phase shift as a function of the applied voltage of the MZI and an inversion of the phase shift for positive and negative voltages are present, these features are not sufficient to conclude that this is indeed due to the Pockels effect. This is explained in [11], which gives an explanation to experimental results obtained for strained Si, which will be shortly summarized, as they are important to interpret experimental results. The main concept there is that the results are a result of the free-carrier plasma effect.

As explained in [11], applying a voltage to the MZI in a single-arm driving configuration leads to a certain phase shift, which is doubled whenever a push-pull configuration is employed. The sign of this phase shift is inverted whenever the applied voltage is inverted. Due to this, we may conclude that the effect responsible for this is a second-order non-linearity in the strained Si. However, some unexpected features are observed. Whenever a voltage above 100 V is applied to an arm of the MZI and left soaking for several minutes, a shift in the phase response is observed, which leads to a hysteresis behavior. Furthermore, in addition to the hysteresis, a variable waveguide attenuation is present and a charging effect can be observed when slow voltage sweeps are performed over extended voltage ranges. For the former, the correlation between the variable attenuation and the phase shift is high, from which we could conclude that the phase shift is due to the free-carrier plasma effect. For the latter, it is seen that performing a voltage sweep after letting the device soak for several minutes at a high voltage, the phase change due to an applied voltage responds quickly in the beginning of the sweep, but after a certain limit, a combination of a semi-instantaneous response followed by a slow response, which partially cancels the fast response, is observed. Therefore, whenever the applied voltage

differs by more than 100 V from the soaking voltage, a slow drift in the response is seen. The effect responsible for the drift is a charging effect in the SiN and the initial fast response is due to charge accumulation in the silicon waveguide.

Both the hysteresis and the drift, which are induced due to the soaking, can be attributed to charging effects. SiN is known to accumulate a surface charge via charged defects, which is usually positively charged. Whenever this SiN-layer is in direct contact with a semiconductor or separated from it through a small silicon dioxide-layer (SiO_2), the polarity can be inverted by applying a high voltage. Therefore, the hysteresis effects occurring when soaking the MZI at a high voltage can be attributed to a mirror charge in the Si waveguide, which builds up as a result of the surface charge in the SiN. Furthermore, the build up of charge in the SiN is responsible for the aforementioned drift after soaking once the polarity of the applied voltage is inverted. Also the linearity of the phase shift when applying a voltage can be explained through the surface charge in the SiN. If we assume that no surface charge is present, the phase shift for positive and negative applied voltages would be of the same polarity, since the former corresponds to accumulation of electrons and the latter of holes at the top surface of the waveguide for sufficiently high voltages, which both reduce the refractive index of the Si. In a push-pull configuration, the resulting phase shift should then be very low. Assuming that the applied voltage is high enough to reach the charge accumulation regime, applying a positive voltage would lead to an accumulation of electrons at the top surface of the waveguide and an accumulation of holes at the bottom surface and vice versa for applying a negative voltage. The total phase shift induced by free carriers would then largely cancel out, but this is not observed experimentally, where a push-pull configuration doubles the phase shift of the single-arm configuration. However, since there is a surface charge present in the SiN, a mirror charge builds up at the top surface of the Si waveguide as a result of this, as explained above. When the surface charge layer in the SiN is positive (by soaking at 0 V or a negative voltage), there will already be an accumulation of electrons at the top surface of the Si waveguide, which is the mirror charge of the positive surface charge in the SiN. Applying a positive voltage will then lead to an increase of the electrons, whereas a negative voltage will lead to a decrease. Therefore, the observed phase shift for positive and negative voltages is reversed. This was also simulated for different values of the surface charge. It was seen that for zero surface charge, the effective index change at 0 V was approximately zero, whereas applying a positive or negative voltage led to a decrease in the effective index, such that both positive and negative voltages have the same polarity. On the other hand, if a non-zero surface charge is present, the effective index change at 0 V is non-zero, which results in an invertible effective index shift.

As reported in [13], a linear effective index variation of the optical mode of a waveguide can also be induced by free carriers or even by trap states and localized charges at the Si/SiN-interface. To investigate whether the response in an interferometer is due to this or due to the Pockels effect, high-frequency measurements were performed on a racetrack resonator in an add-drop configuration, since the Pockels effect and the free-carrier effect have different characteristic times. It was shown that applying a sinusoidal voltage to the electrodes, the value of the induced $\chi^{(2)}$ decreases when the driving bias frequency

increases. At values as small as 4.5 GHz, the $\chi^{(2)}$ disappeared almost completely. Since the linear variation of the effective index induced by the Pockels effect should be able to follow voltage variations instantaneously up to optical frequencies, the effect observed could not be attributed to the Pockels effect. The response was attributed to the free-carrier plasma effect by calculating the free-carrier lifetime.

Due to the free-carrier plasma effect, experimental result should be interpreted carefully, because a wavelength shift in an MZI set-up using strained Si could be the result of the Pockels effect, the free-carrier plasma effect or a combination of both effects.

1.4 All-Optical Switching

In normal switching networks of optical signals, the switching is performed electronically, in which an optical-to-electronic conversion is thus needed. In all-optical switching (AOS) networks, this optical-to electronic conversion would no longer be needed, since the switching would be performed optically. Therefore, AOS in photonic circuits could have a strong impact on high-speed optical communication [18, 19]. The principle of AOS is seen in figure 1, in which an incoming pulse train is switched through an interaction in a nonlinear optical material, either based on self-switching or induced by a control pulse [20]. Since Si is the most used material in microelectronic industry, it would be desired to use Si for such circuits. However, it is difficult to achieve this due to its relatively weak nonlinear optical properties [19].

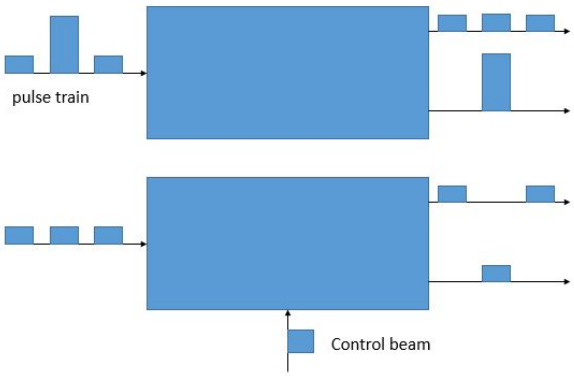

Figure 1: All-optical switching by self-switching (top) and by switching induced by a control pulse (down) [20].

As said before, it is difficult to achieve AOS in Si due to its relatively weak nonlinear optical properties. It has been achieved in Si by using extremely high powers in large or non-planar structures or by using highly light-confining structures to enhance the sensitivity of light to small changes in refractive index, as reported in [19]. The latter is needed because the refractive index and absorption coefficient only show a weak dependence on the free-carrier concentration. To overcome this, highly confined resonant structures were employed, which enhanced the effect of the refractive index change on the transmission

response.

For AOS, the light itself produces the required nonlinear phase shift, which is usually achieved through the intensity dependent refractive index $n = n_0 + n_2 I$ (with n_0 the linear refractive index, n_2 the nonlinear refractive index and I the intensity of the incoming beam), which is a third-order non-linearity [21,22]. However, second-order non-linearities can yield very large effective third-order non-linearities, as long as the condition of nearly phase-matching is achieved for SHG. In non-centrosymmetric materials, as is the case for strained Si, cascaded second-order processes can lead to an effective nonlinear phase shift [20]. Cascading is a process where lower-order effects are combined to contribute to a higher-order nonlinear process, in our case a combination of two second-order nonlinear optical processes that induce a third-order non-linearity. As an example, consider an incoming wave at frequency ω. This wave can generate a wave at the frequency 2ω through SHG. The latter can then subsequently interact with the former to generate a wave at a frequency 3ω through sum-frequency generation (SFG). From the fundamental wave at ω, a wave at 3ω is generated, which can be regarded either as directly generated from third-harmonic generation (THG) or as generated from a combination of SHG and SFG, i.e. cascading of two second-order nonlinear processes. In the case of all-optical switching, the SFG is replaced with difference-frequency generation (DFG), and a wave at the original frequency ω is found, however with a certain nonlinear phase shift. Also, the cascading of optical rectification and subsequently the linear-electro optic effect leads to to a wave at frequency ω with a certain nonlinear phase shift.

As reported in [21], an asymmetric MZI (made of $LiNbO_3$) configuration can be used for AOS. The MZI requires a π relative phase shift between its two arms for switching. Here, the required nonlinear phase difference between both arms was induced by different waveguide widths, due to which the effective mode index and the cross-sectional area will be different. When using temperature tuning for achieving the phase matching condition, both arms require a different phase-matching temperature and hence a different nonlinear phase shift is induced, which is needed for switching at a certain temperature.

An integrated all-optical switch employing the cascaded second-order effect based on an integrated MZI (also made of $LiNbO_3$) is reported in [22]. Due to the use of the cascaded second-order non-linearity, the intensity dependence of the nonlinear phase shift is increased and the sign of it can be controlled by an appropriate choice of phase matching.

An approach for enabling second-order non-linearity and quasi-phase matching (QPM) in Si is reported in [23], based on periodic stress fields in Si. Conventionally poling processes for QPM, as used for e.g. $LiNbO_3$, are not possible for Si, since it lacks a dipole moment in its native form. To achieve periodically poled Si (PePSi), alternating stress fields are created along a Si waveguide using a periodic arrangement of stressed thin films. This breaks the crystal symmetry of Si in a periodic way and a $\chi^{(2)}$ is induced in the structure, while at the same time achieving QPM. The structure of the PePSi consists of a channel waveguide on which tensile stress and compressive stress SiN films are deposited periodically. Due to this, the sign of the stress induced within the Si core alters along the

waveguide, which results in alternating dipole regions. In the tensile stressed part of the waveguide, a compressive stress field is induced and confined inside the waveguide core and the other way around for the compressive stressed part of the waveguide.

2 Simulation Results

The starting point for the study of strained Si are some simulations to compare experimental results with. These are performed with the SILVACO software. With this software, SOI wafers can be generated, after which a SiN layer can be deposited on top of it. The software works with finite-elements method, in which the mesh structure has to defined manually. After defining the desired structure, several operations can be performed on it. For example, an annealing step from a high temperature to room temperature (20°C) can be performed to examine the influence of a temperature step on different parameters of the structure and stress and electric field data can be extracted for further processing with e.g. Matlab. Also a visualisation of the stress and electric field components (or electric field intensity for a certain mode) is possible. In the following sections, several simulations performed with SILVACO are described, in which the used structure is shown, together with the results, generated either with Matlab or SILVACO itself. Two important remarks have to be made with respect to these simulations. The first one deals with the annealing time. SILVACO did not take this time into account, i.e. changing the annealing time did not had any influence on the final results for the stress. Therefore, the same time was used for all annealing steps. The second remark deals with the ramp-up and ramp-down of the annealing. In the beginning of the simulations, first a ramp-up was performed and subsequently a ramp-down, e.g. a ramp-up from 20°C to 800°C was performed, followed by a ramp-down from 800°C to 20°C. Comparing the final result of the combination ramp-up and ramp-down with the result of only a ramp-down, we saw that both had the same final result, i.e. the ramp-down eliminated the effect of the previous ramp-up, such that the ramp-down was the prominent and thus important one. Due to these two remarks, we note that for the following simulations, the annealing time is taken to be constant (10 min) and only ramp-down is considered.

2.1 Annealing in SILVACO

The annealing procedure in SILVACO is performed by using the *DIFFUSION* statement. As explained in the manual, this runs a temperature step on the structure. Furthermore, the method *FULL.CPL* (full coupled) is used, which specifies the type of diffusion equations that has to be used. By adding the method *STRESS.HIST*, stresses are calculated during the diffusion process, in addition to the calculation of the oxidation, silicidation and diffusion of impurities.

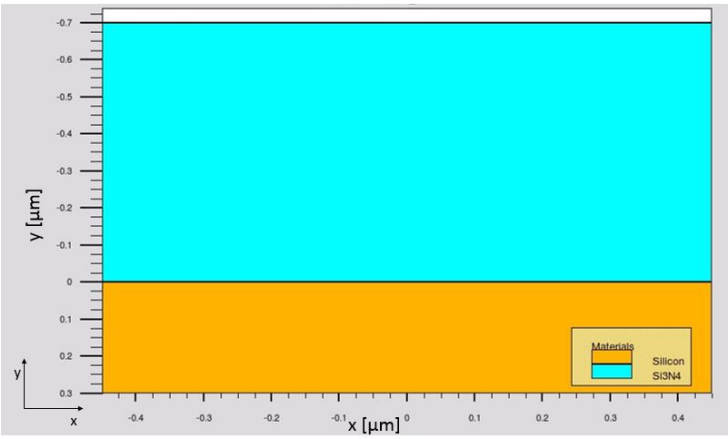

Figure 2: Example of the used structure for the temperature study of the stress across the interface, in this case Si with a 700 nm SiN-layer. For the other structure, only 500 nm was deposited. The structures are subsequently annealed to analyze the stress in the structure as a function of the begin temperature of annealing.

2.2 Temperature Study of the Stress Across the Interface

The first simulation performed with the SILVACO software is to get an idea of how the stress evolves in a structure where Si is capped with a SiN layer and subsequently annealed from a high temperature to room temperature (20°C). The difference in the thermal expansion coefficients between the two different materials will lead to stresses between them when cooled down, especially right at the interface between them [3]. Although the structure simulated here is not a realistic one for use in practical applications, it can give us useful insights in the annealing process performed on the structure. With this simulation, we can see whether, and if so how, the annealing has an influence on the stress inside the Si. For this, a simulation is performed on a Si/SiN-structure, which is subsequently annealed starting from different begin temperatures (400°C, 700°C and 1000°C) to room temperature (20°C). This is done for two different thicknesses of the SiN-layer (500 nm and 700 nm), which allows us to examine whether the thickness of the SiN-layer has an influence on the final stress evolution in the structure, as well as the influence of the begin temperature of annealing on the stress. The deposited SiN-layer is amorphous, in accordance with the PECVD process, which gives rise to amorphous SiN. An example of the structure with a 700 nm SiN-layer is shown in figure 2. At the center of this structure (i.e. at 0 µm on the x-axis), the values of the stress are extracted in the vicinity of the interface (e.g. for y-values close to the interface). Close to this interface, a stress gradient will be present, because the stress in the Si and the one in SiN is different, and we want to study how the stress evolves when crossing the interface. As said before, this stress gradient arises because both materials have a different expansion coefficient and an annealing process will then lead to stresses between them when cooled down. The stress will thus vary from a certain constant value in the bulk Si to another constant value in the bulk SiN. The results of the evolution in the stress when crossing the interface are shown in figures 3, 4 and 5 for a SiN-thickness of 500 nm and 700 nm and for the different stress components (i.e. σ_{xx}, σ_{xy} and σ_{yy} respectively). The x-axis in these figures corresponds with the y-axis in figure 2. The stress without the annealing step is also shown

for comparison.

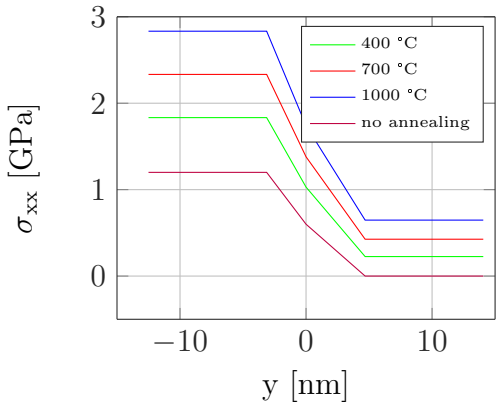

(a) 500 nm

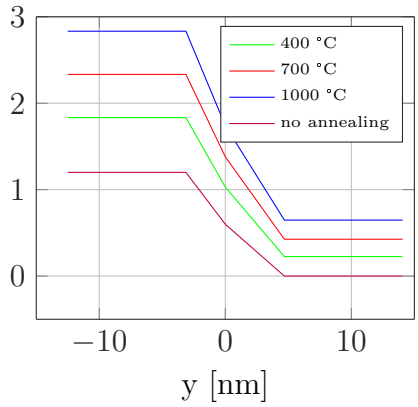

(b) 700 nm

Figure 3: σ_{xx} as a function of distance and begin temperature of annealing at a Si/SiN-interface. y < 0 corresponds with the SiN, y $= 0$ with the interface and y > 0 with the Si.

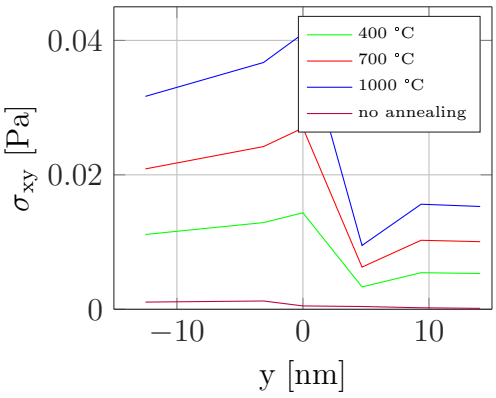

(a) 500 nm

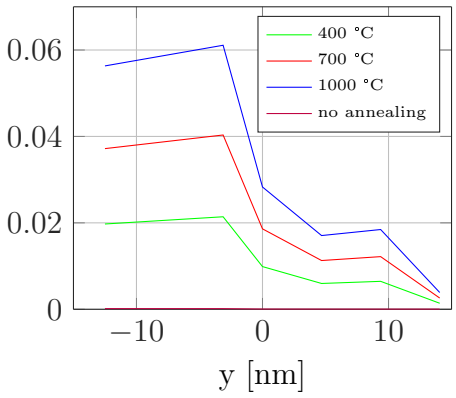

(b) 700 nm

Figure 4: σ_{xy} as a function of distance and begin temperature of annealing at a Si/SiN-interface. y < 0 corresponds with the SiN, y $= 0$ with the interface and y > 0 with the Si.

The first important thing we see when comparing the three figures is that the σ_{xx}-component is the most prominent one, i.e. the σ_{xx}-component (expressed in GPa) is much larger than the σ_{xy}- and σ_{yy}-components (expressed in Pa). Therefore, in the remaining of the discussion and simulations, we will only look at the σ_{xx} component. It is seen that its value only changes significantly in a small layer around the Si/SiN-interface, i.e. only in a region as small as 5 nm on both sides of the interface, while being constant further away from the interface. As said before, this is due to a different expansion coefficients for the Si and SiN. From figure 3, we can also see some other interesting results. First of all, without annealing, the stress in the Si ($y > 0$) evolves towards 0 in the bulk, whereas the

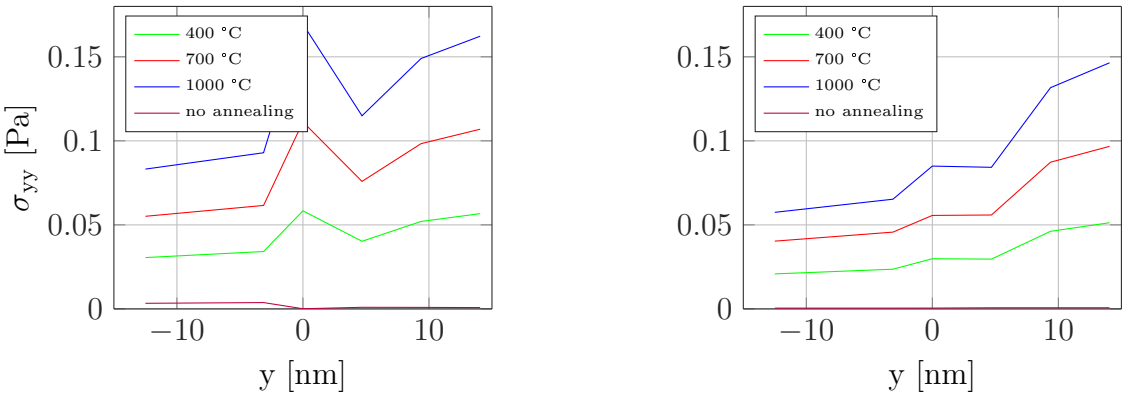

(a) 500 nm **(b)** 700 nm

Figure 5: σ_{yy} as a function of distance and begin temperature of annealing at a Si/SiN-interface. y < 0 corresponds with the SiN, y $= 0$ with the interface and y > 0 with the Si.

stress in the SiN ($y < 0$) evolves towards the intrinsic stress of the nitride, taken to be 1.2 GPa (later on, this value will be changed to look at the influence of the intrinsic stress on the structure). In a small layer around the interface, the stress rapidly increases from the value in the Si towards the one in SiN. Whenever an annealing step is performed on the structure, both the stress values in the Si and in the SiN increase. The region in which the stress changes remains the same, hence the stress gradient in the vicinity of the interface is larger for a higher begin temperature of annealing. This is important since the induced second-order susceptibility $\chi^{(2)}$ is proportional to the strain gradient in the material [13]. Furthermore, the stress increase in the Si is rather small when compared to the one in the SiN. The higher the begin temperature of annealing, the bigger the increase in stress. Another important remark deals with the thickness of the SiN-layer. From the figure, it is clear that there is no significant difference between the stress evolution in both structures when the thickness of the SiN is changed. The values for the σ_{xy}- and σ_{yy}-components do depend slightly on the SiN-thickness, but since the values itself are small compared with the σ_{xx}-component value, they are neglected.

Next, the intrinsic stress of the deposited SiN-layer is changed from $\sigma_1 = 1.2$ GPa (used in the previous simulations) to $\sigma_2 = 10$ MPa and finally to $\sigma_3 = -1.2$ GPa. In practice, this can be done by changing the parameters of the deposition process. When depositing a SiN-layer with PECVD, changing the parameters, such as temperature, pressure, gas chemistry, power density and frequency of the rf excitation source, will have an influence on the stress of the deposited layer [24]. The case of a positive intrinsic stress (σ_1 and σ_2) corresponds with a tensile stress, whereas the case of a negative intrinsic stress (σ_3) corresponds with a compressive stress. Again, the stress components σ_{xy} and σ_{yy} are negligible when compared to the σ_{xx}-component, therefore we only look at the latter. Since the thickness of the SiN-layer only had a small influence on the stress for the σ_{xy}- and σ_{yy}-components (which we discard due to their small values) and was negligible for the σ_{xx}-component, only the case of a 700 nm SiN-layer is simulated. The results for the σ_2- and σ_3-cases are shown in figure 6. In the case of σ_2 (figure 6a), the same behavior as

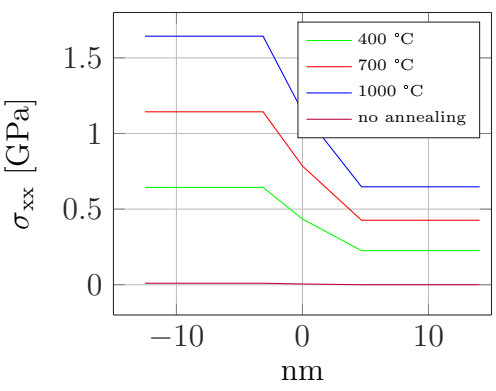

(a) σ_2 = 10 MPa

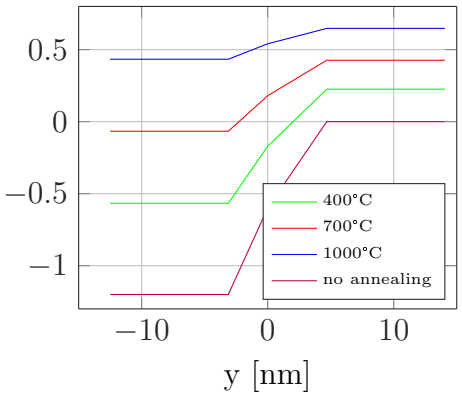

(b) σ_3 = -1.2 GPa

Figure 6: σ_{xx} as a function of distance and begin temperature of annealing at a Si/SiN-interface for variable intrinsic stress of the SiN. y $<$ 0 corresponds with the SiN, y = 0 with the interface and y $>$ 0 with the Si.

for σ_1 is seen (figure 3), i.e. the stress only changes significantly in a small layer around the interface and increases with begin temperature of annealing. When no annealing is performed, the stress in the SiN further away from the interface is the initial intrinsic stress of the SiN used (σ_2 = 10 MPa), whereas the stress in the Si is zero. Furthermore, it is seen that the value for the stress after annealing (at same begin temperature) is smaller compared with the σ_1-case. Hence, a higher initial intrinsic tensile stress leads to a higher stress after annealing. In the case of σ_3 = -1.2 GPa (figure 6b), the result is somewhat different. When no annealing is performed, we see the same behavior, i.e. the stress in the Si is zero and the stress in the SiN evolves towards its intrinsic stress (which is negative in this case). When an annealing process is performed on the structure, the stress in the Si increases. The stress in the SiN goes towards a less negative value (i.e. less compressive), hence the stress is decreasing. After reaching a certain threshold for the begin temperature of annealing, the σ_{xx}-component becomes positive (tensile) and starts to increase towards larger positive values for the stress.

As a conclusion we can say that :

- σ_{xx} is the prominent stress component,
- the influence of the thickness of the SiN-layer is negligible,
- for an intrinsic tensile stress, a higher begin temperature of annealing leads to a higher stress gradient in the vicinity of the interface and a higher initial intrinsic stress leads to a higher stress after annealing and
- for an intrinsic compressive stress, performing an annealing step first lowers the stress and then converts it from compressive to tensile above a certain threshold for the begin temperature.

2.3 Figure of Merit for a Silicon Waveguide Structure

The second simulation is performed on a Si waveguide structure. In this case, a <100>-oriented SOI-wafer is used, after which subsequently a Si waveguide is etched and SiN is deposited on top of this etched structure. The intrinsic stress of the SiN is taken to be $\sigma = 1.2$ GPa. The dimensions of the waveguide structure were optimized in previous work [1]. This optimization is based on the strain gradient and its overlap with the optical mode field inside the waveguide core of the structure. This overlap is evaluated with the following figure of merit (FOM)

$$FOM = \frac{\iint_{WG} |E|^2 \left(\left| \frac{\partial \epsilon_{xx}}{\partial x} \right| + \left| \frac{\partial \epsilon_{xx}}{\partial y} \right| + \left| \frac{\partial \epsilon_{yy}}{\partial x} \right| + \left| \frac{\partial \epsilon_{yy}}{\partial y} \right| \right) dxdy}{\iint_{WG} |E|^2 \, dxdy}. \tag{3}$$

In this equation, E corresponds with the electric field of the optical mode and ϵ_{xx} and ϵ_{yy} are the main strain components. The integration is performed over the waveguide core (WG). This FOM is interesting to look at because it is related with the second-order non-linearity, i.e. the higher its value, the higher the induced non-linearity should be.

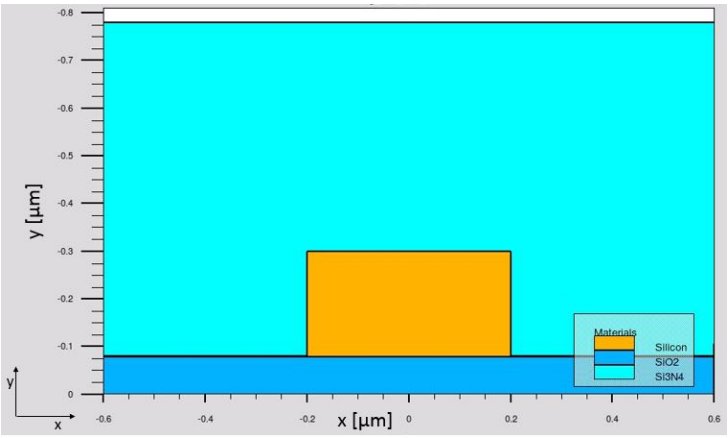

Figure 7: Example of the used structure for the study of the overlap integral in a silicon waveguide. Width w = 400 nm, height h = 220 nm. The structure shown here is with a 700 nm SiN-layer.

The optimized structure from [1] using this FOM for a Si waveguide structure capped with a SiN-layer led to the structure shown in figure 7, created with SILVACO. Both the etch depth and thickness of the SiN-layer were investigated there, with the final result being the structure seen in figure 7, with the dimensions of the waveguide being a width w of 400 nm (x-axis) and a height h of 220 nm (y-axis, standard Si thickness) and a cladding thickness (SiN) of 700 nm.

Using the structure from figure 7, we evaluate the FOM after an annealing step is performed on it. The thickness of the SiN-layer however is changed between 500 nm and

700 nm to see if the thickness of the cladding layer has an influence on the FOM after performing an annealing step. The value of the FOM after annealing is compared with its value at room temperature (as also calculated in [1]) to see whether the temperature step results in an enhanced FOM or not. To calculate the FOM with equation 3, we need the electric field and the strain components in the structure. Therefore, the electric field is calculated with and extracted from SILVACO (both the x- and y-components, at a wavelength of 1.55 µm and both for TE and TM), as well as the stress components σ_{xx}, σ_{xy} and σ_{yy}. These stress components are used to calculate the strain according to following formulas [25]

$$\begin{aligned} \epsilon_{xx} &= 5.91\,10^{-12}\,\sigma_{xx} - 2.77\,10^{-12}\,\sigma_{yy} \\ \epsilon_{yy} &= -2.13\,10^{-12}\,\sigma_{xx} + 7.69\,10^{-12}\,\sigma_{yy} \\ \epsilon_{xy} &= -2.13\,10^{-12}\,\sigma_{xy}. \end{aligned} \tag{4}$$

After extracting everything with SILVACO, the FOM is calculated and visualized with Matlab, as a function of the begin temperature of annealing T_{begin}, as can be seen in figure

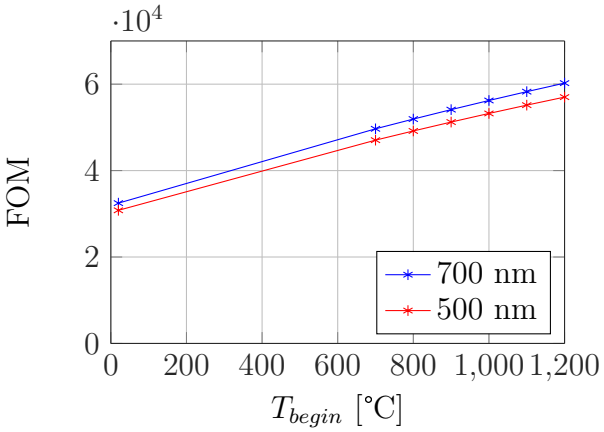

(a) TE

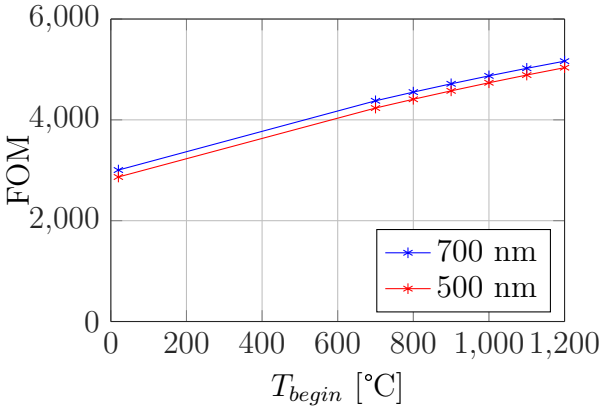

(b) TM

Figure 8: FOM for a Si waveguide structure as a function of begin temperature of annealing and for two different thicknesses of the SiN, both for TE and TM.

8, both for TE and TM and for a thickness of 500 nm and 700 nm of the SiN-layer. A first important remark is that the FOM for the TE case is 10 times larger than in the TM case. Hence, for TE, the induced second-order non-linearity should be higher. Next, we see that performing an annealing step in the structure results in an enhanced FOM, i.e. for a higher begin temperature of annealing, the resulting FOM will also be higher. This can be explained by the fact that a higher begin temperature of annealing leads to higher stress (or higher stress gradients) in the structure due to differences in the thermal expansion coefficients of the materials and therefore, the FOM will become larger [3]. Regarding the influence of the SiN-thickness, we can see that for 700 nm SiN, the FOM is slightly larger than for 500 nm, but compared with the relatively large value of the FOM, the difference is almost negligible. Hence, the SiN-thickness does not have a large impact on the FOM, neither at room temperature nor after annealing. However, we have to note that this only applies whenever the waveguide structure is fully covered with SiN, otherwise the thickness will have an influence, as examined during the optimization of the waveguide structure.

As a conclusion, we can say that for an intrinsic tensile stress :

- the FOM for TE is 10 times larger than the one for TM,
- the induced non-linearity should thus be larger for TE than for TM,
- a higher begin temperature of annealing leads to a higher FOM and
- the thickness of the SiN-layer (500 nm or 700 nm) has a negligible effect on the FOM .

2.4 Figure of Merit for Variable Intrinsic Stress of the Silicon Nitride

As a next simulation, we look at the influence of the intrinsic stress of the deposited SiN-layer, i.e. we look at what happens if this intrinsic stress is changed. In practice, this can be done by changing the parameters of the deposition process [1]. Changing the deposition conditions when depositing SiN with e.g. PECVD also changes the intrinsic stress of the layer, a method which was also used experimentally in [4]. In the same way as before, a Si waveguide is created with a cladding layer of SiN on top of it with a fixed thickness of 700 nm, since the thickness of the SiN had a negligible influence on the FOM (see section 2.3). In the same way as in section 2.2, the intrinsic stress of the SiN is altered between $\sigma_1 = 1.2$ GPa (this value was also used in the previous simulation), $\sigma_2 = 10$ MPa and $\sigma_3 = -1.2$ GPa. Next, an annealing step is performed on the structure and the FOM is calculated. The influence of the annealing and the variable intrinsic stress on the FOM are then examined. Again, the stress and electric field components are extracted from SILVACO and are processed with Matlab to calculate the strain components with equation 4 and then the FOM with equation 3 in the waveguide core. In figure 9, the FOM is shown as a function of the begin temperature of annealing and for the three different intrinsic stress values as given above, both for TE and TM.

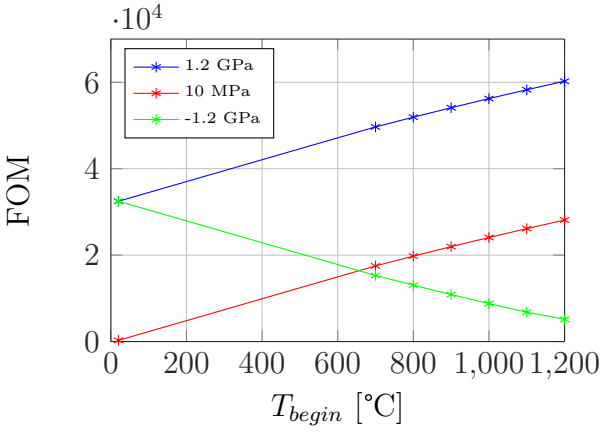

(a) TE

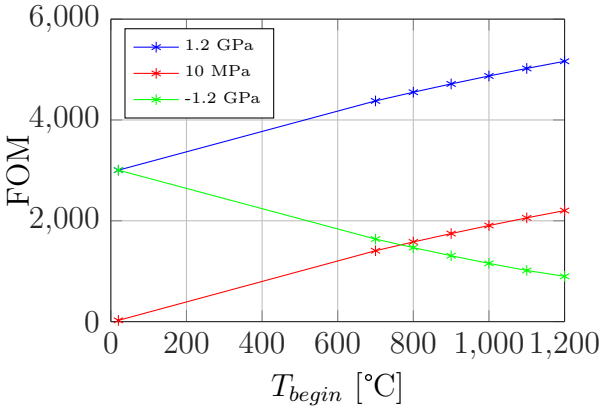

(b) TM

Figure 9: FOM for a Si waveguide structure as a function of begin temperature of annealing and variable intrinsic stress, both for TE and TM.

The graph corresponding with σ_1 (intrinsic tensile stress) is the same one as in the previous section for the case of a 700 nm SiN-layer. From the other two graphs, some interesting conclusions can be obtained. If we look at the σ_2-curve, corresponding with a lower intrinsic tensile stress, we see that its value at room temperature is very small, i.e. as good as negligible compared with the σ_1-case. However, whenever an annealing step is performed, the FOM rises just as fast as in the σ_1-case. The only drawback is that to achieve a value which is comparable to the value in the σ_1-case at room temperature, annealing temperatures of 1200°C or even higher need to be used. Therefore, using a higher intrinsic tensile stress would be preferred when wanting to achieve a FOM as high as possible. If we now look at the σ_3-curve, corresponding with an intrinsic compressive stress, we see that at room temperature its FOM is approximately the same as in the σ_1-case, but after annealing, its value decreases as fast as the value in the σ_1-case increases. Therefore, higher annealing temperatures lead to a lower FOM and vice versa. The explanations given above for the σ_2- and σ_3-curves apply both for TE and TM. Again, the FOM for the TE-case is 10 times larger than the one for the TM-case.

As a conclusion, we can say that

- lowering the intrinsic tensile stress leads to a decrease in FOM,
- performing an annealing on a structure with intrinsic tensile stress enhances the FOM, whereas for intrinsic compressive stress the FOM decreases and
- the best FOM after annealing is achieved for a high intrinsic tensile stress.

2.5 Silicon Waveguide for Second-Harmonic Generation Experiments

As described in [5], the method of a strained SiN-layer to demonstrate SHG was recently used successfully. Silicon waveguides with dimensions 10 µm by 2 µm were made, covered with SiN with different stress extent, stress sign and layer thickness to investigate the influence of the stress on SHG. A 2.1 µm pump source was used, and due to SHG, a signal at the wavelength 1.05 µm was generated. Based on this, we run a simulation for a 10 µm by 2 µm Si waveguide with 4 µm SiN on top of it. Next, modal transmission in this waveguide structure is examined for wavelengths of 1.05 µm, 1.55 µm and 2.1 µm, i.e. we look if the waveguide structure is single-mode or multi-mode at the observed wavelengths. According to [26], the number of modes in a rectangular waveguide can be approximated by

$$N_{rect} \approx \frac{\pi\, b}{2\, a} \left(\frac{f}{f_o^{rect}} \right)^2, \tag{5}$$

in which a is the wide dimension of the waveguide, b the narrow dimension and $f_o^{rect} = c/2a$ the cut-off frequency. Using a = 10 µm, b = 2 µm and f the frequency corresponding with one of the above wavelengths ($f = c/\lambda$), we find that the waveguide supports approximately 114, 52 and 28 modes for the different wavelengths respectively. Note however that this equation is an approximation since the refractive indices of the used materials are not used in this equation. Therefore, the value obtained for the number of modes is an estimation, which should approximately be the right number, but some

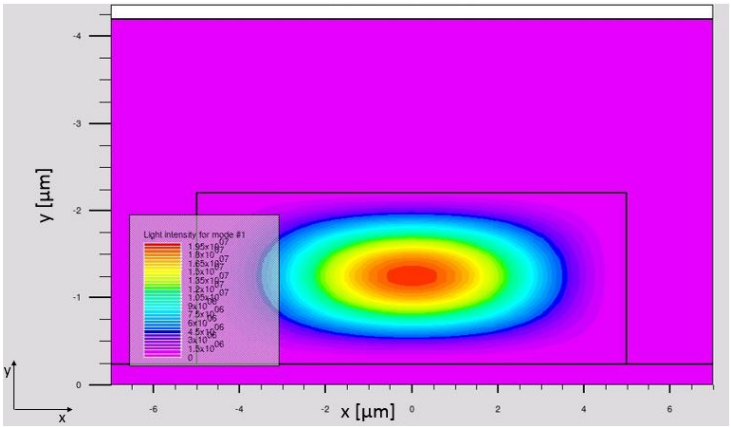

Figure 10: Intensity distribution in the SHG waveguide structure for the lowest order mode, corresponding with a TE mode.

variation on this number can be expected. Nevertheless, the waveguide is multi-mode for all the considered wavelengths. This could be expected since the used wavelengths are much smaller compared with the dimensions of the waveguide. With the SILVACO software, the electric field values can be extracted or it can be visualized for the lowest order modes (the maximum mode number is defined by the user, e.g. when you insert 4, the first 4 modes are calculated). After visualization of the electric field intensity of a higher order mode, it is clear that it is indeed multi-mode, since the higher-order modes are still guided by the waveguide. Next, the first-order mode, corresponding with a TE-mode, is used to calculate the overlap integral in the waveguide core. The light intensity in the waveguide for the lowest order mode is shown in figure 10. From this, it can be seen that the mode is situated in the center of the waveguide structure, it is not present at the edges of the structure and it is guided. In figure 11, the stress component σ_{xx} in the waveguide structure is shown after an annealing step starting from 700°C. Comparing both figures, it can be seen that in the center of the structure, where the intensity is highest, the stress is approximately constant, with a value around 0.1 GPa. The highest stress gradients are found near the edges of the structure. The bad overlap between the intensity and the stress gradient explains why the FOM, as seen in figure 12 as a function of begin temperature of annealing and wavelength, is rather low in the structure. Although the intensity distribution was shown for the TE-mode, the same applies for the TM-mode, i.e. a bad overlap between the intensity and stress gradient for TM also results in a low FOM. Some important differences with the FOM here and the ones from sections 2.3 and 2.4 can be seen. Whereas in the previous sections the FOM for the TE-case was ten times larger than the one for the TM-case, here both are approximately of the same order in this structure. Moreover, the order of magnitude is relatively small compared with the previous sections, due to less overlap between the intensity and high regions of stress. As said before, the FOM is shown for wavelengths of 1.05 µm, 1.55 µm and 2.1 µm. The influence of the wavelength on the FOM, both for TE and TM, is rather low, although the influence for TE is somewhat bigger. Nevertheless, the wavelengths do not have a strong influence on the FOM.

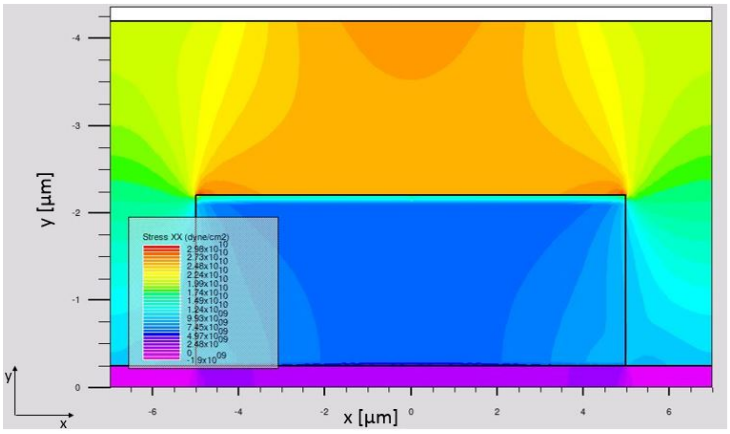

Figure 11: σ_{xx} in the SHG waveguide structure.

As a conclusion, we can say that

- the FOM is rather low,
- the difference in FOM between TE and TM is negligible and
- the influence of the wavelength on the FOM is negligible.

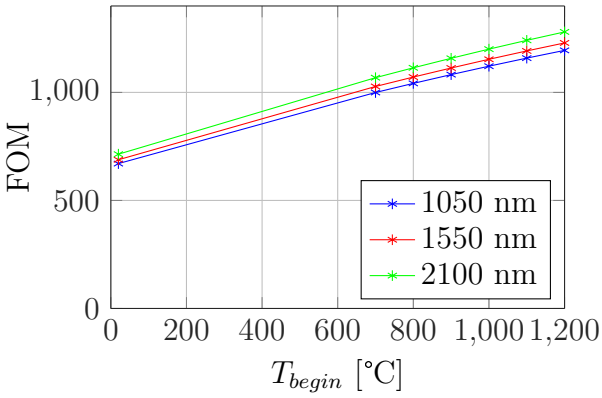

(a) TE

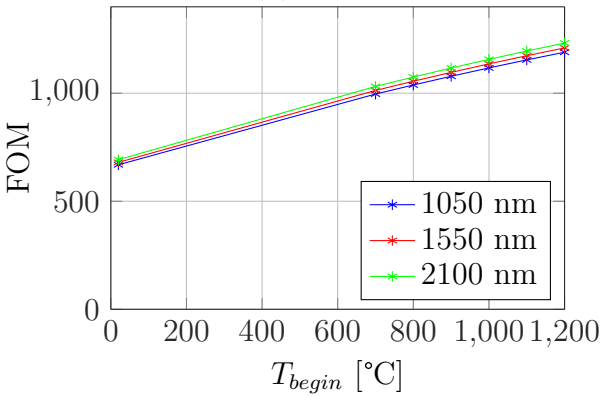

(b) TM

Figure 12: FOM for a SHG waveguide structure as a function of begin temperature of annealing and wavelength.

2.6 Smaller Waveguide for Second-Harmonic Generation

Since the structure described in section 2.5 is rather big for waveguides, we now investigate if we could use a smaller waveguide for the SHG experiment at $\lambda = 2.1$ µm. More specifically, we investigate if we could design a waveguide for SHG experiments with a height h of 220 nm (standard Si thickness) as seen in the sections 2.3 and 2.4 with a 700 nm SiN-cladding layer. Using a smaller waveguide allows us to bring the regions of high stress gradient (the edges of the waveguide) and high electric field intensity (center of the waveguide core) closer to each other, and hence increasing the FOM. In order to find out

if we could use a certain waveguide for SHG experiments, the structure needs to have at least one guided mode at the highest wavelength used (λ = 2.1 µm), because for lower wavelengths, more guided modes will be present. Therefore, we make use of equation 5, which we transform to the following form

$$N_{rect} \approx \frac{2\pi ab}{\lambda^2}. \tag{6}$$

Again, we point out that this equation is only an approximation, since the refractive indices do not appear in it, and therefore, an interpretation of the result should be done carefully. Since the height h of the waveguide is fixed to 220 nm, the values of a and b depend on the width w of the waveguide, i.e. if w is smaller than 220 nm, then a = h = 220 nm and b = w, otherwise a = w and b = h = 220 nm. If we use w = 400 nm, as before, we find with equation 6 a value of 0.125 for the number of modes. When visualizing the electric field intensity with SILVACO, the mode is seen to be present in the waveguide core, with a considerable amount present in the upper cladding. To move the intensity more to the center of the waveguide, the width can be increased. Therefore, we take b = 220 nm and a = w. If we solve equation 6 with N_{rect} = 1 to find a, we get that a $\approx$ 3.19 µm. Hence, a waveguide with w = 3.19 µm and h = 220 nm will have one guided mode and the intensity will be centered in the waveguide and could be used for SHG experiments. Since the used equation was only an approximation, other waveguide widths were also simulated, from 3 µm to 2.7 µm and the intensity was plotted. Here, it was seen that the intensity was not spreading more in the cladding and hence smaller widths for the waveguide are possible, which in addition have a better confinement. Therefore, the above equation is not suitable to calculate single-mode condition. The fact that waveguides with other widths are more suitable for SHG experiments can also be seen from the FOM. After simulating, the FOM is found to be approximately 1.398 10^4 for TE at room temperature at λ = 2.1 µm, which is approximately 3 times smaller than the values for the original waveguide (see section 2.3), but still significantly larger than the values of figure 12. Due to this, we have a confirmation that the waveguide indeed could be used for SHG experiments, since the higher FOM should induce a higher non-linearity, but the higher FOMs calculated in the previous sections prove that these waveguides are more suitable for SHG experiments. The width of the waveguide should thus be optimized by looking at the FOM. More simulations need to be performed for this.

Although the calculated width of 3.19 µm is not the optimal value for it, as explained above, the influence of annealing and the thickness of the SiN-layer on the FOM are examined. The annealing is performed in the same temperature range as before (700°C - 1200°C) and the thickness of the SiN-layer is changed between 500 nm and 700 nm. Also the influence of the different wavelengths, as given before, on the FOM is examined. In figure 13, the FOM is shown, for TE, as a function of begin temperature of annealing for the different SiN-layer thicknesses and for the different wavelengths. From the figure, it can be seen that increasing the begin temperature of annealing leads to a higher FOM, hence a higher non-linearity should be induced. Looking at a fixed begin temperature of annealing, the FOM is slightly larger for a 700 nm SiN-layer than for a 500 nm SiN-layer. The wavelength now also has a clear influence on the FOM, with a higher wavelength leading to a higher FOM (at a fixed temperature).

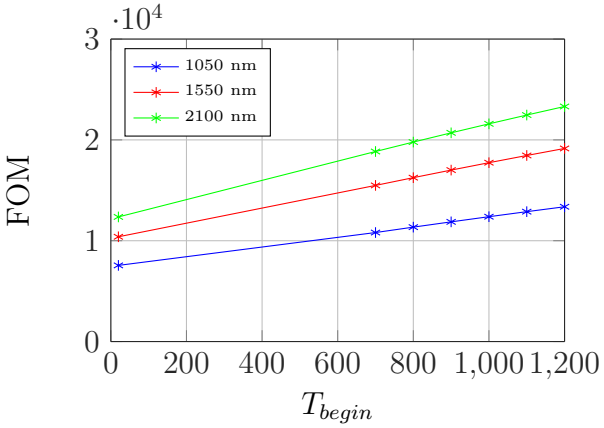

(a) 500 nm

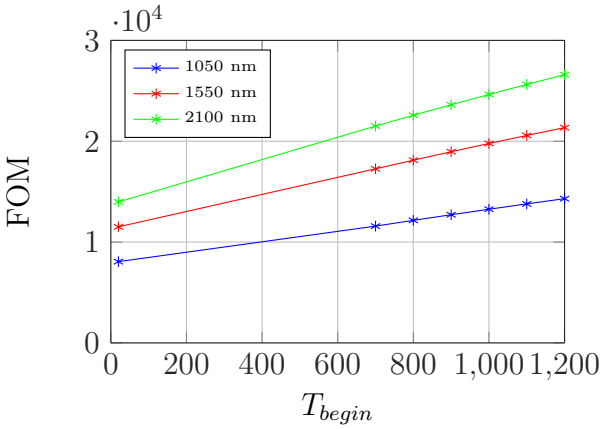

(b) 700 nm

Figure 13: FOM for a SHG waveguide as a function of begin temperature of annealing, thickness of the SiN-layer and wavelength for TE and for waveguide dimensions w = 3.19 µm and h = 220 nm.

As a conclusion, we can say that

- the smaller waveguide dimensions increase the FOM,
- annealing increases the FOM,
- the wavelength has a clear influence on the FOM, with a higher wavelength leading to a higher FOM and
- the influence of the thickness of the SiN-layer on the FOM is negligible.

3 Experimental Results

After the simulations, some experiments are performed to compare with the results from the simulations. As already explained in section 1.1, strained silicon can be employed for

optically active devices relying on the second-order non-linearity, such as an MZI, which makes use of the Pockels effect. However, as explained in section 1.3, the experimental results obtained in an MZI set-up of strained silicon do not confirm the fact that these are a result of the Pockels effect, since also the free-carrier plasma effect should be taken into account.

The experimental set-up consists of an asymmetrical MZI of which the waveguides are fabricated in Si and are covered with a SiN-straining layer through PECVD. Hence, the deposited SiN-layer is amorphous, as was also the case in the simulations. On top of the long arm of the MZI, aluminium (Al) electrodes are deposited to apply a voltage, such that we work in the single-arm driving configuration. The MZI is designed to work in the TE-mode through the coupling gratings. An optical signal (tunable laser between 1540 nm and 1585 nm) is injected into the MZI at 0 dBm and the optical output power is measured with a photodetector. Two different MZIs are employed : one with an arm length of 4 mm ($\Delta L = 50\mu$m) and one with an arm length of 1 mm with the same ΔL.

3.1 High-Stress Sample

To start the experiment, the MZIs as explained above are fabricated, i.e. Si waveguides are deposited with a SiN stressing layer through PECVD. In this section, the intrinsic stress of the SiN is -2 GPa, i.e. an intrinsic compressive stress, which is achieved through proper deposition parameters of the PECVD process. Different experiments are performed on this sample, as explained in the following sections.

3.1.1 Influence of Annealing

In the first experiment, a cycle from 0 to 120 V to -120 V and back to 0 V is performed with steps from 30 V, both before and after annealing, to examine the influence of annealing on the response of the MZI. Since we work with a sample with an intrinsic compressive stress, we expect a decrease in the FOM after annealing, as was seen in figure 9 in the simulations. Therefore, the induced non-linearity and the corresponding response of the MZI should become smaller, at least if the response of the MZI can be attributed to the Pockels effect. The annealing was performed at a temperature of 500°C for 30 minutes. On the obtained experimental graphs, a Fourier fitting of the first-order is plotted to extract the values of the resonance wavelengths, since an MZI response is proportional with a cosine. The values for the resonance wavelength peaks before (λ_{before}) and after (λ_{after}) annealing at the different applied voltages are given in table 1. It has to be noted here that different resonance peaks were used to calculate the resonance wavelengths. This however has no limitation to compare the results before and after annealing, as the shift in resonance wavelength relative to the one at 0 V at the beginning of the cycle is calculated, as seen in figure 14.

As said before, according to the simulations, the FOM after annealing should decrease, as is seen in figure 9. When we assume that the FOM defined in equation 3 is proportional

Table 1: Resonance wavelengths of an MZI with arm length of 4 mm ($\Delta L = 50\,\mu m$) for a voltage sweep from 0 V to 120 V to -120 V to 0 V, before and after annealing, for a high-stress sample. The values were obtained through a Fourier fitting of the first order.

Voltage [V]	λ_{before} [nm]	λ_{after} [nm]
0	1550.7	1569
30	1550.5	1567.3
60	1550.3	1565.9
90	1549.4	1564.3
120	1548.8	1563.2
90	1550.2	1564.6
60	1551.1	1566.1
30	1551.1	1567.9
0	1551.2	1569.7

Voltage [V]	λ_{before} [nm]	λ_{after} [nm]
-30	1552.4	1570.9
-60	1552.9	1571.8
-90	1553	1572.1
-120	1553.1	1568.4
-90	1552.5	1567.9
-60	1552.1	1567.9
-30	1552.1	1568.0
0	1551.3	1567.4

to the change in effective index Δn_{eff}, which in turn is proportional to the change in wavelength through the equation $\frac{\Delta\lambda}{\lambda} = \frac{\Delta n_{eff}}{n_g}$, with n_g the group index of Si, both the change in wavelength and the FOM are proportional to the change in effective index and they can be related with each other. Although the simulation was performed for σ = -1.2 GPa and the experiment was performed on a sample with σ = -2 GPa, the results of the simulation can give us an insight in what should happen after annealing. Therefore, a linear interpolation is performed in figure 9 between 20°C and 1200°C to calculate the value of the FOM at 500°C. Taking the ratio of the FOM at the annealing temperature of 500°C and the one at room temperature, we find

$$\frac{FOM_{500^\circ\mathrm{C}}}{FOM_{20^\circ\mathrm{C}}} \approx \frac{21350.70}{32464.14} \approx 0.66. \tag{7}$$

This learn us that the decrease in performance, if it is due to the Pockels effect, should be around 0.66.

When we now look at the experimental result (see figure 14), the maximum wavelength shift before annealing is approximately $\Delta\lambda \approx 2.4\,\mathrm{nm} - (-1.9\,\mathrm{nm}) = 4.3\,\mathrm{nm}$ and after annealing $\Delta\lambda \approx 3.1\mathrm{nm} - (-5.8\mathrm{nm}) = 8.9\mathrm{nm}$. On a first sight, the annealing thus improves the response. To examine the influence of the annealing on the relative wavelength shift, we fit a linear curve to the experimental curves of figure 14. For the curve before annealing, the slope of the fitted curve is approximately -0.01728. For the curve after annealing, only the linear part is taken (between 0 V to 120 V to -30 V), which gives us a slope of approximately -0.05197. Hence, the influence of the annealing can be calculated by taking the ratio of both slopes, which gives us

$$\frac{-0.05197}{-0.01728} \approx 3.0075, \tag{8}$$

which gives us an improved slope of a factor 3 after annealing.

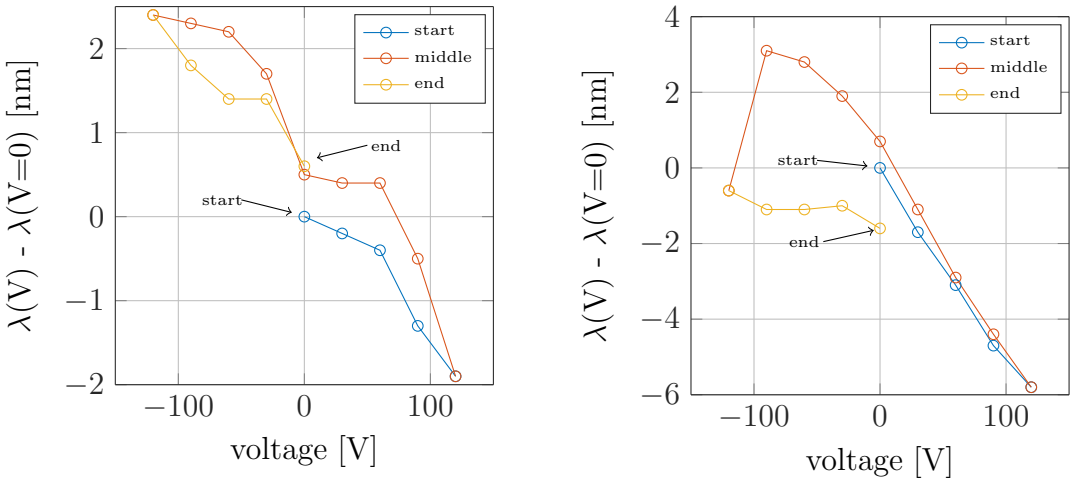

(a) before annealing

(b) after annealing

Figure 14: Resonance wavelength of an MZI with an arm length of 4 mm ($\Delta L = 50\,\mu m$) relative to the one at 0 V for a voltage sweep from 0 V to 120 V to -120 V to 0 V, before and after annealing, for a high stress sample. The start and end point are indicated. After the start point, the cycle follows the blue curve ('start'), next the red curve ('middle') and finally the yellow curve ('end') until the end point.

Two important remarks with respect to figure 14 have to be made. The first one has to do with the fact that the response around 0 V is not symmetrically, i.e. for positive voltages, the wavelength shift after annealing is larger than for negative voltages, and the other way around before annealing. The second remark deals with the peak seen in figure 14b. At a certain voltage level (-90 V), the shift in resonance wavelength reverses polarity, i.e. instead of increasing further to higher wavelengths, it reverses towards lower wavelengths, leading to a peak in the wavelength shift. The explanation of both remarks is found in section 1.3, which deals about the free-carrier plasma effect. Also seen is that the peak is only clearly observed when going from positive to negative voltages, due to which we think that the peak when going from negative to positive voltages is either centered at a larger negative voltage or not clearly visible in the obtained graph. Nevertheless, a hysteresis behavior arises. Before annealing, this peak is not observed. However, this does not mean that it is not present, but we think that the peak would probably be at a larger negative voltage, which according to [11] corresponds with a larger positive surface charge in the SiN.

On the one hand, we expect from the simulations a decrease in the response since the FOM decreases after annealing. On the other hand, the experiments learn us that the response is increased after annealing, which can be seen through a larger resonance wavelength shift and thus a larger slope for the response. Hence, the simulation and experiment are contradicting. Due to all of the above, we are not able to conclude whether the response after annealing is due to a presence of the Pockels effect or due to a combination between the Pockels effect and the free-carrier plasma effect.

Table 2: Resonance wavelengths of an MZI with an arm length of 4 mm ($\Delta L = 50\,\mu m$) for three consecutive cycles (voltage sweeps) from 0 V to 120 V to -120 V to 0 V, after annealing, for a high-stress sample. The values were obtained through a Fourier fitting of the first order.

Voltage [V]	$\lambda_{\text{cycle 1}}$ [nm]	$\lambda_{\text{cycle 2}}$ [nm]	$\lambda_{\text{cycle 3}}$ [nm]
0	1567.9	1565.7	1565.3
30	1566.1	1564.2	1564.4
60	1564.0	1563.2	1563.2
90	1562.2	1562	1562
120	1560.6	1560.9	1560.9
90	1562.8	1562.4	1562.5
60	1564.8	1564	1563.9
30	1566.8	1566	1566
0	1568.2	1567.3	1567.5

Voltage [V]	$\lambda_{\text{cycle 1}}$ [nm]	$\lambda_{\text{cycle 2}}$ [nm]	$\lambda_{\text{cycle 3}}$ [nm]
-30	1568.6	1568.9	1568.9
-60	1568.5	1568.8	1568.8
-90	1566.8	1567.5	1567
-120	1565.7	1566	1565.9
-90	1565.7	1565.6	1565.7
-60	1566.1	1565.8	1566
-30	1566.2	1566	1566.2
0	1565.7	1565.3	1565.9

Next, the same cycle as above is performed, three consecutive times, but three days after the annealing was performed. We perform three cycles to see whether the result is reproducible and we perform the experiment after three days to see whether the influence of annealing is still present after a certain time instead of directly after annealing. The values of the resonance wavelength peaks as a function of the applied voltage and cycle are shown in table 2, again obtained through a Fourier fitting of the first order. The visualization of these values is shown in figure 15, relative to the resonance wavelength at 0 V, for the three cycles. Comparing the figures for the different cycles with figure 14b performed directly after the annealing, approximately the same shape of the cycle is seen. Hence, after three days, the annealing procedure performed on the sample still has its influence on the response of the MZI.

Looking at figure 15, we see that the first cycle differs only very small from the two next cycles. The second and third cycles have approximately the same behavior. For the first cycle, the start curve (blue) and the the middle curve (red) cancel each other out between 0 V and 120 V. When reversing the voltage to negative values, the resonance shift first goes towards longer wavelengths, i.e. in the reverse direction as for positive voltages, but beyond -60 V, the wavelength shift reverses again and goes towards shorter wavelengths. Notice that the voltage at which this peak occurs is smaller than in the case directly after annealing. The reverse shift when going from positive to negative values is expected if the response is the result from the Pockels effect. Since the free-carrier plasma effect could also be responsible for the linearity and reverse shift in the resonance wavelength, as explained in the previous experiment and in section 1.3, we are again not able to conclude whether the Pockels effect is observed or not. The free-carrier plasma effect also explains the peak observed, as explained in the previous experiment, due to surface charges in the SiN. The same behavior is seen even after performing several cycles, hence the response is reproducible. Again, the peak is clearly present when going from

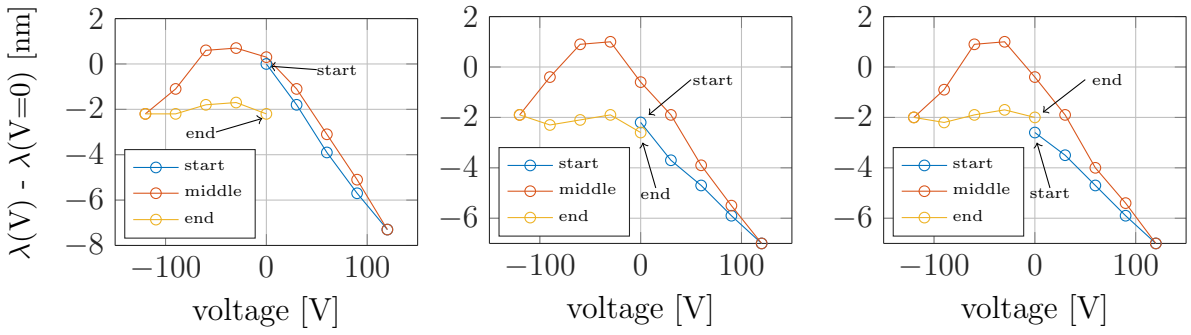

(a) cycle 1 **(b)** cycle 2 **(c)** cycle 3

Figure 15: Resonance wavelength relative to the one at 0 V of an MZI with an arm length of 4 mm ($\Delta L = 50$ µm) for three consecutive cycles (voltage sweeps) from 0 V to 120 V to -120 V to 0 V, after annealing, for a high stress sample. The start and end points are indicated. After the start point, the cycle follows the blue curve ('start'), next the red curve ('middle') and finally the yellow curve ('end') until the end point.

positive to negative voltages and not clearly observed in the reverse sweep, therefore we think that the peak for the latter either would be situated at a larger negative voltage or is not observed clearly in the obtained graph. As explained before, this results in a hysteresis behavior as seen in the figure.

Next, an MZI with an arm length of 1 mm is used ($\Delta L = 50$ µm) and the same cycle is performed, both before and after annealing. In table 3, the values for the resonance wavelengths at each applied voltage throughout the cycle is shown, both before (λ_{before}) and after (λ_{after}) annealing, obtained through a Fourier fitting of the first order. In figure

Table 3: Resonance wavelengths for an MZI with an arm length of 1 mm ($\Delta L = 50$ µm) for a voltage sweep from 0 V to 120 V to -120 V to 0 V, both before and after annealing, for a high-stress sample. The values were obtained through a Fourier fitting of the first order.

Voltage [V]	λ_{before} [nm]	λ_{after} [nm]
0	1552.4	1562.3
30	1552.2	1561.9
60	1552.2	1561.5
90	1552	1561.1
120	1552	1560.7
90	1552.1	1561.3
60	1552	1561.8
30	1552.4	1562.2
0	1552.6	1562.4

Voltage [V]	λ_{before} [nm]	λ_{after} [nm]
-30	1552.8	1562.8
-60	1553	1562.4
-90	1553	1562
-120	1553.1	1561.8
-90	1552.9	1562
-60	1552.7	1562
-30	1552.4	1562
0	1552.2	1561.8

16, these resonance wavelengths with respect to the one at the beginning of the cycle at 0 V is shown. As can be seen, the maximum wavelength shift is $\Delta\lambda = 0.7 - (-0.4) = 1.1$ before annealing and $\Delta\lambda = 0.5 - (-1.6) = 2.1$ after annealing. From this, an improvement in the wavelength shift is seen after annealing. Again, the peak and the corresponding reverse in the wavelength shift are observed at a negative voltage due to the free-carrier plasma effect. Also, the peak is not observed before annealing, which again does not imply that it is not present, but probably would be situated around larger negative voltages. In accordance with the MZI with an arm length of 4 mm, the slopes of the linear parts of the figures are calculated through a linear fitting to the data. Before annealing, a slope of -0.004944 is found. After annealing, only the first part between 0 and 120 V is used, and the slope is found to be -0.01383. Hence, the influence of annealing on the slope is found to be

$$\frac{-0.01383}{-0.004944} \approx 2.7973, \tag{9}$$

which is smaller than the improvement factor for the longer MZI. Again, the experiment shows an improvement in the response, whereas the simulations showed us a decrease in FOM and hence response.

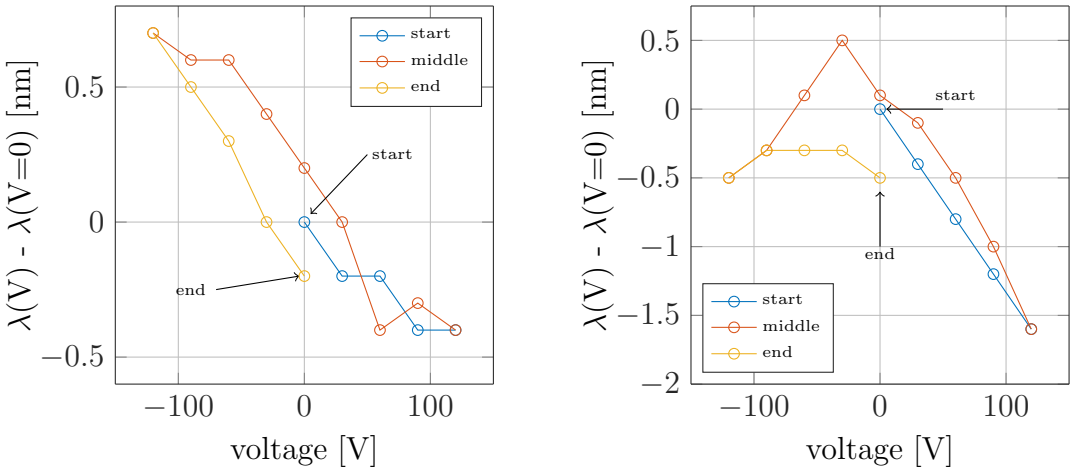

(a) before annealing **(b)** after annealing

Figure 16: Resonance wavelength relative to the one at 0 V of an MZI with an arm length of 1 mm ($\Delta L = 50\,\mu m$) for a voltage sweep from 0 V to 120 V to -120 V to 0 V, before and after annealing, for a high stress sample. The start and end points are indicated. After the start point, the cycle follows the blue curve ('start'), next the red curve ('middle') and finally the yellow curve ('end') until the end point.

3.1.2 Influence of Soaking at -120 V

In the next experiment, the MZI is left soaking at -120 V for 10 minutes, after annealing, and a voltage sweep to 120 V and back to -120 V is performed, with steps of 30 V. The MZI response, i.e. the output power as a function of wavelength, for the MZI with an arm

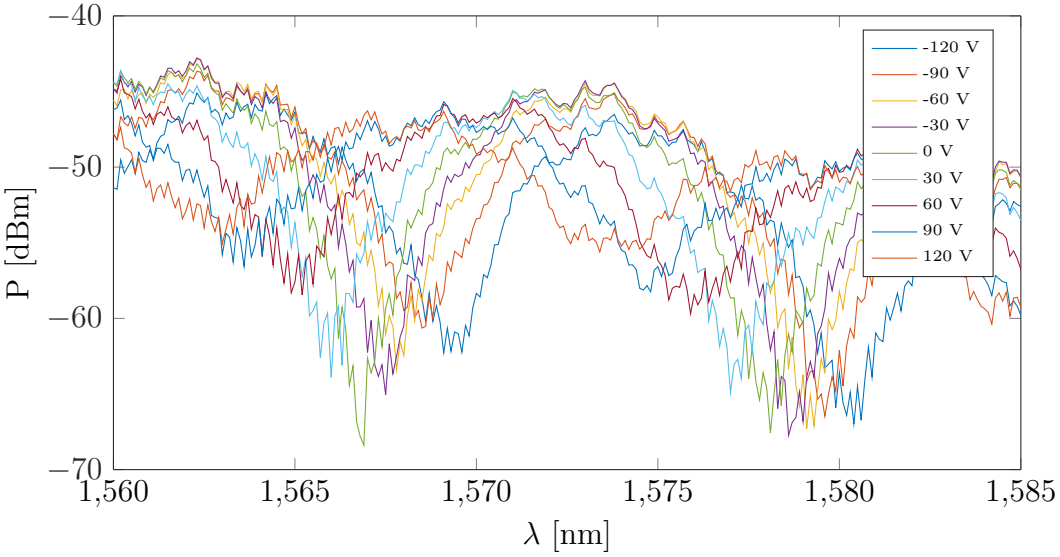

(a) -120 V → 120 V

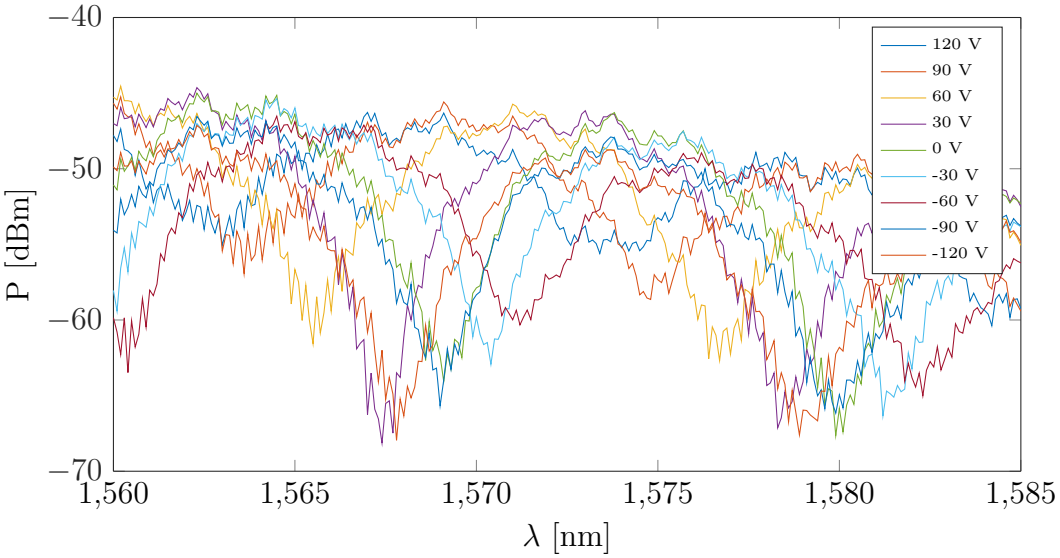

(b) 120 V → -120 V

Figure 17: Output power as a function of wavelength (= MZI response) for an MZI with an arm length of 4 mm ($\Delta L = 50$ µm) after soaking at -120 V for 10 minutes and after annealing for a high-stress sample for (a) voltage sweep from -120 V to 120 V and (b) voltage sweep from 120 V back to -120 V.

length of 4 mm ($\Delta L = 50$ µm) after soaking and annealing during the voltage sweep is shown in figure 17. From this, the resonance wavelengths are obtained through a Fourier fitting of the first order, for both resonance peaks ($\lambda_{res,1}$ and $\lambda_{res,2}$) observed, as seen in table 4. The visualization of these resonances relative to the resonance wavelength at 0 V (the first time 0 V was reached, i.e. 1567.2 nm for peak 1 and 1578.3 nm for peak 2, see table 4) is shown in figure 18. Also shown in this figure is the curve from figure 14b corresponding with the relative wavelength shift after annealing without soaking, such

that the influence of soaking at -120 V after annealing can be examined.

Table 4: Resonance wavelengths for an MZI with an arm length of 4 mm ($\Delta L = 50\,\mu m$) after soaking at -120 V for 10 minutes, for a voltage sweep from -120 V to 120 V to -120 V, after annealing, for a high-stress sample. The values were obtained through a Fourier fitting of the first order.

Voltage [V]	$\lambda_{res,1}$ [nm]	$\lambda_{res,2}$ [nm]
-120	1569.3	1580.8
-90	1568.6	1580.0
-60	1568.1	1579.4
-30	1567.7	1578.9
0	1567.2	1578.3
30	1566.4	1577.4
60	1565.3	1576.5
90	1563.8	1575.0
120	1562.1	1574.0

Voltage [V]	$\lambda_{res,1}$ [nm]	$\lambda_{res,2}$ [nm]
90	1564	1575.2
60	1565.9	1577.0
30	1567.6	1578.8
0	1569.2	1580.3
-30	1570.6	1581.6
-60	1571.6	1582.2
-90	1569.2	1580.2
-120	1567.9	1579.3

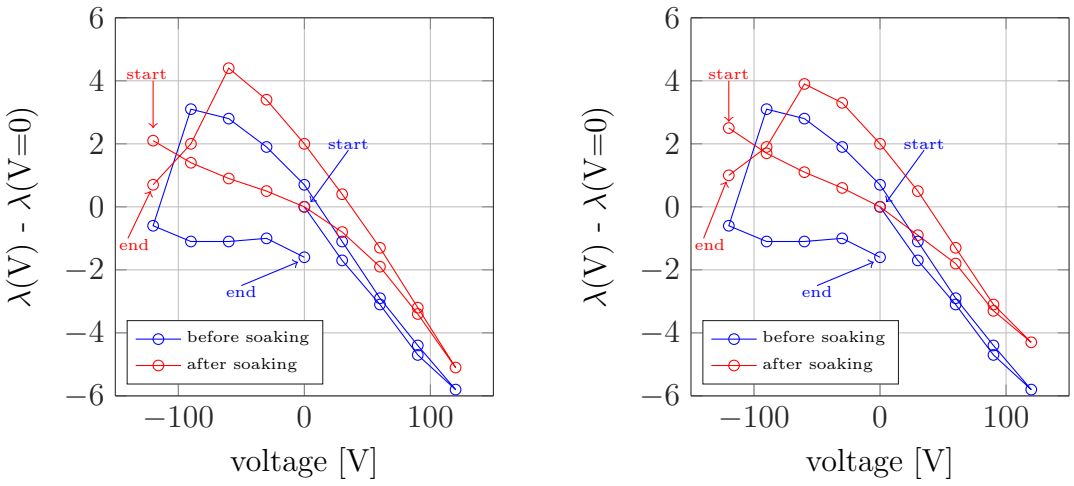

(a) peak 1 **(b)** peak 2

Figure 18: Resonance wavelength relative to the one at 0 V of an MZI with an arm length of 4 mm ($\Delta L = 50\,\mu m$) for a voltage sweep, before and after soaking at -120 V, for a high stress sample. Before soaking, the voltage sweep was performed from 0 V to 120 V to -120 V to 0 V. After soaking, the voltage sweep was performed from -120 V to 120 V to -120 V. The start and end points for both cases are indicated.

As can be seen from the figure, the cases before and after soaking show similar characteristics. For example, the slopes in the linear parts of both curves are approximately the same and some hysteresis can be seen. Also the influence of the free-carrier plasma effect is present both before and after soaking, as can be seen seen from the peaks in both

Table 5: Resonance wavelengths for an MZI with an arm length of 4 mm ($\Delta L = 50\,\mu m$) after soaking at 120 V for 10 minutes, for a voltage sweep from 120 V to -120 V to 120 V, after annealing, for a high-stress sample. The values were obtained through a Fourier fitting of the first order.

Voltage [V]	λ_{res} [nm]
120	1561.1
90	1562.9
60	1565.0
30	1566.9
0	1568.1
-30	1568.4
-60	1568.2
-90	1567.2
-120	1566.1

Voltage [V]	λ_{res} [nm]
-90	1565.9
-60	1566.1
-30	1566.1
0	1565.7
30	1564.2
60	1563.0
90	1561.4
120	1560.2

curves for negative voltages. However, the voltage at which this peak occurs differs before and after soaking, i.e. after soaking, this voltage shifts to a smaller negative voltage. Also seen is that the wavelength at which this peak occurs shifts to a larger value after soaking.

3.1.3 Influence of Soaking at 120 V

In the following experiment, the MZI (arm length 4 mm, $\Delta L = 50\,\mu m$) was left soaking at 120 V for 10 minutes, after annealing, and a voltage sweep to -120 V and back to 120 V is performed, with steps from 30 V. From the MZI response of this cycle, the resonance wavelengths are extracted at the different applied voltages through a Fourier fitting of the first order, which are given in table 5. The visualization of these resonances relative to the resonance wavelength at 0 V (the first time 0 V was reached, i.e. 1568.1 nm; see table 5) is shown in figure 19. In accordance with section 3.1.2 about soaking at -120 V, the curve from figure 14b corresponding with the relative wavelength shift after annealing without soaking is also shown in figure 19, in order to examine the influence of soaking at 120 V after annealing.

As can be seen from the figure, again the same characteristics are seen before and after soaking. Both curves have approximately the same slope in their linear parts, a hysteresis is present and the influence of the free-carrier plasma effect is observed, as is seen by the peak when going from positive to negative voltages. Again, the voltage at which this peak occurs after soaking at 120 V is shifted to a smaller negative value when compared to the case before soaking. The wavelength at which the peak occurs is now shifted to a smaller value after soaking at 120 V, whereas before, after soaking at -120 V, it was shifted to a larger value.

3.1.4 Conclusion

The influence of annealing and soaking, both at a negative voltage of -120 V and at a positive voltage of 120 V, for a high-stress sample were examined. In the case of annealing, the simulations predicted a decrease in FOM with a factor 0.66. The experimental results however gave an improvement of about 3. Hence, the simulation and the experiment are contradictory. Before annealing, no peak in the relative resonance wavelength is seen, whereas after annealing, a clear peak is observed, resulting from the free-carrier plasma effect. This does not mean that this effect is not present before annealing, but we think that the peak should be centered around a larger negative voltage. The shift towards a smaller negative voltage after annealing could be explained by the fact that an annealing procedure decreases the surface charge in the SiN due to a decrease in the defects in the SiN after annealing.

Comparing the cases of soaking at -120 V and 120 V with the case without soaking, all three after annealing, some remarkable results are seen. For both soaking cases, the voltage at which a peak is observed in the relative resonance wavelength shift attributed to the free-carrier plasma effect is shifted to a smaller negative value when compared to the case without soaking. Also, the wavelength at which this peak occurs shifts when compared to the wavelength before soaking, to a larger wavelength after soaking at -120 V and to a smaller wavelength after soaking at 120 V. When looking at the peak, we see that it occurs for a negative voltage. According to simulations performed and according to [11], this means that a positive surface charge is present in the SiN. As explained in section 1.3, a mirror charge in the Si arises, i.e. negative electrons accumulate at the top surface of it. For soaking at 120 V, more electrons are accumulated there. These electrons are actually decreasing the surface charge in the SiN to a smaller positive value

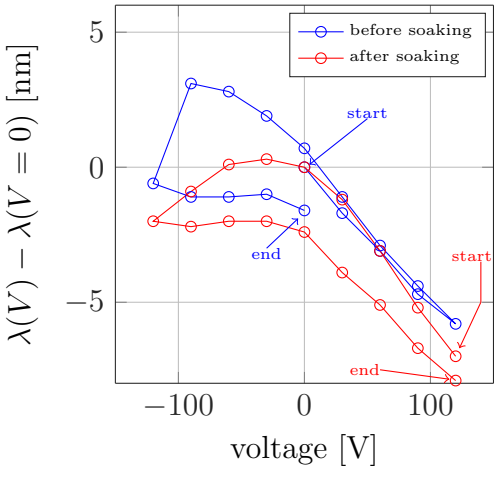

Figure 19: Resonance wavelength relative to the one at 0 V of an MZI with an arm length of 4 mm ($\Delta L = 50\,\mu m$) for a voltage sweep, before and after soaking at 120 V, for a high stress sample. Before soaking, the voltage sweep was performed from 0 V to 120 V to -120 V to 0 V. After soaking, the voltage sweep was performed from 120 V to -120 V to 120 V. The start and end points for both cases are indicated.

or even to negative values whenever the applied voltage is large enough, which should shift the peak to smaller negative values of the voltage, as was also seen after performing some simulations about this. For soaking at -120 V, the existing electron accumulation is reduced, which increases the surface charge in the SiN and hence should shift the peak towards larger negative values of the voltage. The expected behavior for soaking at a positive voltage is confirmed in the experiments, but the expected behavior for soaking at a negative voltage however is not observed, more remarkable, the reverse behavior is seen. More simulations with respect to the free-carrier plasma effect should be performed to clearly understand the behavior that is observed.

3.2 Low-Stress Sample

In this section, the MZIs as described before are employed, but the intrinsic stress of the SiN stressing layer now has a value of -30 MPa, i.e. a compressive intrinsic stress, which is smaller than in the previous section. Again, this is achieved through a proper choice of the PECVD process parameters.

3.2.1 Influence of Annealing

In accordance with section 3.1.1 in the high-stress sample, the influence of annealing on the MZI response in the low-stress sample is examined for the MZI with an arm length of 1 mm ($\Delta L = 50\,\mu m$). A voltage sweep is performed on the sample to see a possible shift in resonance wavelength. In table 6, the values for the resonance wavelengths of the MZI before annealing (λ_{before}) as a function of the applied voltage are shown, obtained through a Fourier fitting of the first order, in accordance with the previous section. In table 6a, these resonances are shown starting from 0 V and going to -120 V, i.e. going to negative voltages. Since no shift in the resonance wavelength was observed, only two positive voltages, 60 V and 120 V were applied, for which also no shift was seen. In table

Table 6: Resonance wavelengths for an MZI with an arm length of 1 mm ($\Delta L = 50\,\mu m$) for two different voltage sweeps before annealing, for a low-stress sample. The values were obtained through a Fourier fitting of the first order.

Voltage [V]	λ_{before} [nm]
0	1555.2
-30	1555.3
-60	1555.2
-90	1555.3
-120	1555.2
0	1555.3
60	1555.4
120	1555.3

(a) measurement 1

Voltage [V]	λ_{before} [nm]
0	1555.2
30	1555.3
60	1555.3
90	1555.3
120	1555.3
0	1555.2
-60	1555.1
-120	1555.0

(b) measurement 2

6b, the resonance wavelengths starting from 0 V and going to 120 V, i.e. to positive voltages, are shown. Again, no shifts in the resonance wavelengths were seen, due to which only two negative voltages were applied, for which again no shift was seen. Although no simulations were performed for a lower intrinsic compressive stress, the same behavior as for a lower intrinsic tensile stress could be expected, i.e. a shift of the curve of the high intrinsic compressive stress towards lower values of the FOM. The FOM then would be almost zero at room temperature, due to which a possible induced Pockels effect would also be small. Due to this, no shift in resonance wavelength is observed.

Table 7: Resonance wavelengths for an MZI with an arm length of 1 mm ($\Delta L = 50\,\mu m$) for a voltage sweep from 0 V to 120 V to -120 V and for two different soaking times at -120 V, after annealing, for a low-stress sample. The values were obtained through a Fourier fitting of the first order.

Voltage [V]	λ_{after} [nm]
0	1554.1
30	1554.0
60	1554.0
90	1554.0
120	1554.0
90	1554.0
60	1554.0
30	1554.0

Voltage [V]	λ_{after} [nm]
0	1554.0
-30	1554.1
-60	1554.0
-90	1554.0
-120	1553.9
-120 soaking 5 min	1553.9
-120 soaking 20 min	1553.9

In the same way as before, an annealing was performed on the sample at 500°C for 30 minutes, and the MZI response was measured again. In this case, a voltage sweep from 0 V to 120 V to -120 V was performed, with steps of 30 V. The corresponding values for the resonance wavelengths are given in table 7, obtained through a Fourier fitting of the first order. No shift in the resonance wavelength is seen, as was also the case before annealing. Remarkable however is that no influence of the free-carrier plasma effect is seen. To ensure that this effect is not present, the MZI was left soaking at -120 V and the MZI response was measured after 5 minutes of soaking and after 20 minutes. As explained before, soaking the device at a large value leads to a shift in the peak observed in the effective index change (or relative resonance wavelength shift) [11], due to which the resonance wavelength should change. As can be seen in table 7, the soaking however had no influence on the resonance wavelength.

In accordance with the simulations of section 2.4 for an intrinsic compressive stress, a decrease of the FOM is expected after annealing. Since already no response was seen before annealing, also no response after should be seen, as is the case.

3.2.2 Conclusion

The influence of annealing for a low-stress sample was examined. Before annealing, no shift in resonance wavelength was observed. Assuming a shift of the high intrinsic compressive stress curve to lower values of the FOM, this could be expected. After annealing, the FOM would be even smaller and thus also no response should be seen, as confirmed by the experiment. Remarkable however is the fact that also no influence of the free-carrier plasma effect is observed, which was clearly present in the high-stress sample. Therefore, both the Pockels effect and the free-carrier plasma effect are not clearly present in the low-stress sample.

4 Summary

Since the crystal structure of Si is centro-symmetric, second-order non-linearities are not present in Si. However, as showed in several references, straining Si with a SiN-layer can break this symmetry and then second-order non-linearities could be induced in the Si. Several simulations were performed on this so-called strained Si. According to simulations of the temperature study at a Si/SiN-interface, performing an annealing on the structure increased the stress in the vicinity of the interface in the case of SiN with an intrinsic tensile stress and decreased it in the case of SiN with an intrinsic compressive stress. Next, a figure of merit (FOM) was defined, the value of which is related with the second-order non-linearity, i.e. the higher its value, the higher the induced non-linearity should be. Looking at the FOM for a Si waveguide strained with SiN with an intrinsic tensile stress, an increase in FOM was seen when the begin temperature of annealing was increased. Hence, the induced non-linearity should be higher after performing an annealing on a structure with SiN with an intrinsic tensile stress. The influence of the thickness of the SiN-layer on the value of the FOM was almost negligible. When decreasing the value of the intrinsic tensile stress of the SiN, the curve of the high intrinsic tensile stress shifted towards lower values of the FOM, i.e. a lower intrinsic tensile stress led to a lower FOM than for a high intrinsic tensile stress, both before and after annealing. When changing the intrinsic stress from tensile to compressive, the reverse behavior was seen : the FOM decreased when an annealing was performed on the structure. Several simulations for a waveguide suitable for SHG were performed and the width of this waveguide was altered to ensure that the guide mode present at a wavelength of $\lambda = 2.1$ µm was centered in the waveguide core.

For the experimental part, an asymmetrical MZI in Si strained with an intrinsic compressive stress SiN-layer was fabricated. Experiments were performed both on a high-stress and a low-stress sample. For both of them, the influence of annealing on the response was examined. This was examined by comparing the response before and after annealing for a voltage sweep, with both positive and negative voltages. Although the simulations predicted a decrease in FOM, and hence also in response, we saw an improvement of the response for the high-stress sample, and no difference at all for the low-stress sample. Furthermore, for the high-stress sample, clear evidence of the free-carrier plasma

effect was seen, as was seen through a peak in the relative resonance wavelength shift at a negative voltage. This was only observed after annealing and not before annealing. This however does not imply that it is only present after annealing, but we believe that the peak before annealing is centered around a larger negative voltage. Since the position of this peak depends on the surface charge in the SiN, where a large positive surface charge corresponds to a peak centered around a large negative voltage and a large negative surface charge corresponds to a peak around a large positive voltage, it is thus believed that annealing reduces the surface charge, i.e. from a large positive surface charge to a lower positive one. This peak was only observed when going from positive to negative voltages and not vice versa, which led to a hysteresis behavior in the response. Also when several consecutive voltage sweeps were performed three days after annealing, the response stayed the same. Hence, reproducibility of the response is possible. Also for an MZI with a smaller arm length, the same behavior, although with a smaller response, was observed. Next, the influence of soaking, both at -120 V and 120 V, was compared with the case before soaking. Although the relative wavelength shift before and after soaking was comparable, some differences were observed. For both soaking states, the peak resulting from the free-carrier effect shifted to a lower negative voltage, hence it is believed that the soaking reduces the surface charge in the SiN. For the soaking at 120 V, this shift towards a smaller negative value was expected, but for soaking at -120 V, a shift towards a larger negative voltage was expected. Furthermore, for soaking at -120 V, the wavelength at which the peak occurs shifted towards a larger value, whereas for soaking at 120 V, the shift was towards a smaller value.

5 Acknowledgement

The author would like to thank following persons :

Prof. Pablo Sanchis, being the supervisor of the master thesis, for providing the subject, infrastructure, help and advice to successfully complete it.

Irene Olivares, PhD-student at NTC and daily supervisor, for the help with the simulations, experimental work, processing and interpretation of the results.

Friends and family, as being a mental support.

References

[1] I. Olivares, T.I. Angelova, E. Pinilla-Cienfuegos, and P. Sanchis. A systematic optimization of design parameters in strained silicon waveguides to further enhance the linear electro-optic effect. SPIE Photonics Europe, Brussels (Belgium), 2016.

[2] L. Pavesi. Silicon photonics course from HELIOS project [online]. URL : http://www.helios-project.eu/Download/Silicon-photonics-course [accessed 23 May 2016].

[3] C. Schriever, C. Bohley, J. Schilling, and R. B. Wehrspohn. Strained silicon photonics. *Materials*, 5(5):889, 2012.

[4] Pedro Damas, Xavier Le Roux, David Le Bourdais, Eric Cassan, Delphine Marris-Morini, Nicolas Izard, Thomas Maroutian, Philippe Lecoeur, and Laurent Vivien. Wavelength dependence of pockels effect in strained silicon waveguides. *Opt. Express*, 22(18):22095–22100, Sep 2014.

[5] C. Schriever, F. Bianco, M. Cazzanelli, M. Ghulinyan, C. Eisenschmidt, J. de Boor, A. Schmid, J. Heitmann, L. Pavesi, and J. Schilling. Second-order optical nonlinearity in silicon waveguides: Inhomogeneous stress and interfaces. *Advanced Optical Materials*, 3(1):129–136, 2015.

[6] M. Cazzanelli, F. Bianco, E. Borga, G. Pucker, M. Ghulinyan, E. Degoli, E. Luppi, V. Vniard, S. Ossicini, D. Modotto, S. Wabnitz, R. Pierobon, and L. Pavesi. Second-harmonic generation in silicon waveguides strained by silicon nitride. *Nature Materials*, 11(2), February 2012.

[7] Matteo Galli, Dario Gerace, Karl Welna, Thomas F. Krauss, Liam O'Faolain, Giorgio Guizzetti, and Lucio Claudio Andreani. Low-power continuous-wave generation of visible harmonics in silicon photonic crystal nanocavities. *Opt. Express*, 18(25):26613–26624, Dec 2010.

[8] Q. Lin, J. Zhang, G. Piredda, R. W. Boyd, P. M. Fauchet, and G. P. Agrawal. Dispersion of silicon nonlinearities in the near infrared region. *Applied Physics Letters*, 91(2), 2007.

[9] Li Chen, Qiang Xu, Michael G. Wood, and Ronald M. Reano. Hybrid silicon and lithium niobate electro-optical ring modulator. *Optica*, 1(2):112–118, Aug 2014.

[10] S. V. Govorkov, V. I. Emel'yanov, N. I. Koroteev, G. I. Petrov, I. L. Shumay, and V. V. Yakovlev. Inhomogeneous deformation of silicon surface layers probed by second-harmonic generation in reflection. *J. Opt. Soc. Am. B*, 6(6):1117–1124, Jun 1989.

[11] S. Sharif Azadeh, F. Merget, M. P. Nezhad, and J. Witzens. On the measurement of the pockels effect in strained silicon. *Opt. Lett.*, 40(8):1877–1880, Apr 2015.

[12] R.S. Jacobsen, K.N. Andersen, P.I. Borel, J. Fage-Pedersen, L.H. Frandsen, O. Hansen, M. Kristensen, A.V. Lavrinenko, G. Moulin, H. Ou, C. Peucheret, B. Zsigri, and A. Bjarklev. Strained silicon as a new electro-optic material. *Nature*, 441:199–202, 2006.

[13] M. Borghi, M. Mancinelli, F. Merget, J. Witzens, M. Bernard, M. Ghulinyan, G. Pucker, and L. Pavesi. High-frequency electro-optic measurement of strained silicon racetrack resonators. *Opt. Lett.*, 40(22):5287–5290, Nov 2015.

[14] Tingyin Ning, Henna Pietarinen, Outi Hyvrinen, Janne Simonen, Gory Genty, and Martti Kauranen. Strong second-harmonic generation in silicon nitride films. *Applied Physics Letters*, 100(16), 2012.

[15] Kazuhiro Ikeda, Robert E. Saperstein, Nikola Alic, and Yeshaiahu Fainman. Thermal and kerr nonlinear properties of plasma-deposited silicon nitride/silicon dioxide waveguides. *Opt. Express*, 16(17):12987–12994, Aug 2008.

[16] Jacob S. Levy, Mark A. Foster, Alexander L. Gaeta, and Michal Lipson. Harmonic generation in silicon nitride ring resonators. *Opt. Express*, 19(12):11415–11421, Jun 2011.

[17] S. Lettieri, S. Di Finizio, P. Maddalena, V. Ballarini, and F. Giorgis. Second-harmonic generation in amorphous silicon nitride microcavities. *Applied Physics Letters*, 81(25), 2002.

[18] Andrew M. C. Dawes, Lucas Illing, Susan M. Clark, and Daniel J. Gauthier. All-optical switching in rubidium vapor. *Science*, 308(5722):672–674, 2005.

[19] Vilson R. Almeida, Carlos A. Barrios, Roberto R. Panepucci, and Michal Lipson. All-optical control of light on a silicon chip. *Nature*, 431:1081–1084, 2004.

[20] Christian Bosshard. Cascading of second-order nonlinearities in polar materials. *Advanced Materials*, 8(5):385–397, 1996.

[21] Y. Baek, R. Schiek, G. I. Stegeman, G. Krijnen, I. Baumann, and W. Sohler. All-optical integrated machzehnder switching due to cascaded nonlinearities. *Applied Physics Letters*, 68(15), 1996.

[22] C. N. Ironside, J. S. Aitchison, and J. M. Arnold. An all-optical switch employing the cascaded second-order nonlinear effect. *IEEE Journal of Quantum Electronics*, 29(10):2650–2654, Oct 1993.

[23] Nick K. Hon, Kevin K. Tsia, Daniel R. Solli, and Bahram Jalali. Periodically poled silicon. *Applied Physics Letters*, 94(9), 2009.

[24] Kenneth Mackenzie, David Johnson, Michael DeVre, Russell Westerman, and Brad Reelfs. Stress control of si-based pecvd dielectrics. *Meeting Abstracts*, MA2005-01(9):406, 2006.

[25] M. A. Hopcroft, W. D. Nix, and T. W. Kenny. What is the young's modulus of silicon? *Journal of Microelectromechanical Systems*, 19(2):229–238, April 2010.

[26] P. V. Nikitin, D. D. Stancil, and E. A. Erosheva. Estimating the number of modes in multimode waveguide propagation environment. In *Antennas and Propagation (APSURSI), 2011 IEEE International Symposium on*, pages 1662–1665, July 2011.

A Articles

Influence of Annealing for Enhancing Second-Order Nonlinearity in Strained Silicon

Steven Van Roye, Irene Olivares, Pablo Sanchis*

Nanophotonics Technology Center, Universitat Politècnica de València, Spain

*pabsanki@ntc.upv.es

Second-order optical nonlinearity can be induced in silicon (Si) by breaking the crystal symmetry with a straining layer [1,2]. The influence of annealing for enhancing the nonlinearity by means of a silicon nitride (SiN) layer is investigated. The annealing process has been simulated taking into account different begin temperatures to room temperature. Furthermore, the influence of the intrinsic stress and thickness of the SiN layer has also been analyzed. To start with, SiN deposited on top of a Si substrate was considered and the stress when crossing the interface was obtained. Figure 1(a) shows that the stress in the Si ($y > 0$) is zero and increases in a small layer around the interface to the intrinsic stress 1.2 GPa of the SiN ($y < 0$). Whenever an annealing step is performed, both the stress in the Si and in the SiN increases, but the increase in the SiN is larger than in the Si. Therefore, a higher begin temperature of annealing leads to higher stress around the interface. Next, a figure of merit (FOM) has been defined as the normalized overlap integral over the waveguide core between the electric field intensity and partial derivatives of the strain components, since the value of this FOM will be proportionate with the induced nonlinearity. The dimensions of the waveguide (height = 220 nm, width = 400 nm) were optimized in previous work [3]. From the simulations, it was found that the FOM for TE was ten times larger than the one for TM, therefore only the TE is considered here. Figure 1(b) shows the FOM as a function of the begin temperature of annealing for a SiN-thickness of 500 nm and 700 nm. In the latter, the FOM is slightly larger than in the former, although the difference is quite small. We also see that an annealing procedure starting from a higher temperature leads to a higher FOM and therefore to a larger non-linearity. In Figure 1(c), the FOM is plotted as a function of begin temperature of annealing for a 700 nm SiN-layer, but the intrinsic stress of this layer is changed from 1.2 GPa (as before) to 10 MPa and to -1.2 GPa. The case of 10 MPa shows the same behaviour as the case of 1.2 GPa, but the FOM is significantly smaller. For -1.2 GPa, the FOM at room temperature is equal to the 1.2 GPa case, but performing an annealing step leads to a lower FOM. As a conclusion, a combination of annealing and compressive intrinsic stress of the SiN layer will be beneficial to enhance the induced second-order optical nonlinearity in silicon.

References

[1] R. Jacobsen et al., Nature 441(7090), 199–202 (2006).

[2] M. Cazzanelli et al., Nat. Mater. 11(2), 148–154 (2011).

[3] I. Olivares, T.I. Angelova, E. P.-Cienfuegos, P. Sanchis, SPIE Photonics Europe, Brussels (Belgium), 2016.

Figures

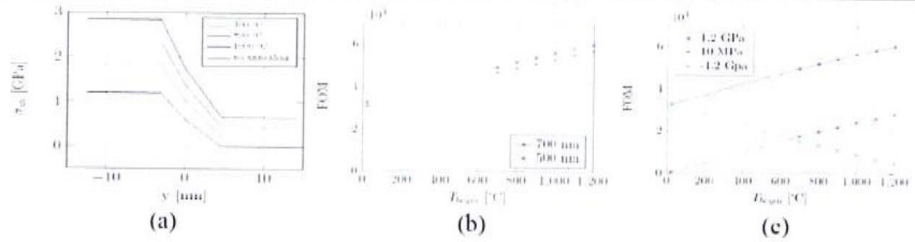

(a) (b) (c)

Figure 1: (a) Stress xx as a function of distance perpendicular to the interface for no annealing, 400°C, 700°C and 1000°C (from bottom to top), (b) FOM as a function of begin temperature of annealing for 500 nm and 700 nm SiN –layer, (c) FOM as a function of begin temperature of annealing for different intrinsic stresses of the SiN.